SKS and *SPdKS* sensitivity to two-dimensional ultralow-velocity zones

Stéphane Rondenay,[1] Vernon F. Cormier,[2] and Emily M. Van Ark[1]

[1]   Seismic wave propagation through two-dimensional core-mantle boundary (CMB) ultralow-velocity zones (ULVZs) is modeled using a global pseudospectral algorithm. Seismograms are synthesized for several types of ULVZ models to investigate the effect of these structures on *SKS* and *SPdKS* phases. One-dimensional models and two-dimensional models with different, quasi-1-D velocity structures on the source and receiver sides of the CMB provide a baseline for comparison with other 2-D models. Models with finite length ULVZs are used to test the sensitivity of the *SPdKS* travel time and waveform to different portions of the *P* diffracted wave path. This test shows that *SPdKS* waves are only sensitive to ULVZs with lengths >100 km. Our results give three tools for identifying and characterizing 2-D ULVZ structures. First, dual *SPdKS* pulses indicate exposure to at least two separate CMB velocity structures, either different source and receiver-side CMB velocities or different adjacent velocity regions for which P_{diff} inception occurs outside of and propagates into a ULVZ. Second, high-amplitude *SKS* precursors indicate a very "strong" (i.e., thick and/or large velocity perturbations) ULVZ. Hence, the absence of *SKS* precursors in most previous ULVZ studies indicates that very strong, sharp ULVZs are not common. Third, mean *SPdKS* delays relative to PREM constrain the minimum ULVZ strength and length combinations required to produce a given travel time delay.

1.   Introduction

[2]   The boundary between Earth's liquid, mostly iron outer core and its solid silicate mantle spans contrasts in density, chemical composition, and viscosity as great as those found at the surface of the Earth between the solid crust and the fluid ocean and atmosphere [*Jeanloz and Williams*, 1998]. There is evidence of significant thermal and chemical heterogeneity at multiple scale lengths in this core-mantle boundary (CMB) region [*Bataille et al.*, 1990; *Cormier*, 2000; *Garnero*, 2004]. Large-scale (hundreds to thousands of kilometers) structures probably related to mantle downwelling (subduction) and upwelling (the Pacific and African "superplumes") have been observed at the bottom of the mantle using seismic tomography [*van der Hilst et al.*, 1998; *Grand*, 2002; *Trampert and van der Hilst*, 2005] and have been inferred from geodynamic models of mantle convection [*Tackley*, 1998; *Tackley et al.*, 2005; *van Thienen et al.*, 2005]. The existence of very small scale (micrometers to millimeters) compositional and phase variation near the CMB are suggested by high-pressure mineral physics experiments [*Knittle*, 1998; *Murakami et al.*, 2004; *Shim*, 2005] and models [*Wentzcovitch et al.*, 1995; *Bukowinski and Akber-Knutson*, 2005]. The intermediate spatial scales can affect the waveforms of seismic body waves. Characterizing CMB complexity at all of these scales is key to understanding the dynamics of the Earth's interior.

[3]   Here we focus on ultralow-velocity zones (ULVZs): thin (2 to 40 km thick) regions of mantle just above some portions of the CMB that are characterized by large *P* and *S* wave velocity reductions. There are several proposed explanations for low velocities in ULVZs. The most common hypothesis is the presence of partial melt [*Williams and Garnero*, 1996; *Revenaugh and Meyer*, 1997; *Helmberger et al.*, 1998; *Vidale and Hedlin*, 1998; *Williams et al.*, 1998; *Zerr et al.*, 1998; *Berryman*, 2000; *Wen*, 2000; *Ross et al.*, 2004]. Variations in chemical composition on the mantle side of the CMB [*Manga and Jeanloz*, 1996; *Stutzmann et al.*, 2000], "sediments" of finite rigidity collecting on the top of the outer core [*Buffett et al.*, 2000; *Rost and Revenaugh*, 2001], and a gradient in the mantle-core transition (rather than the traditional sharp CMB) [*Garnero and Jeanloz*, 2000a, 2000b] have also been proposed, alone and in combination. More recently, *Mao et al.* [2006] proposed that iron enrichment in the postperovskite phase [*Murakami et al.*, 2004] might account for ULVZs.

[4]   There are several seismic phases that are very sensitive to CMB structure that have been used to test many areas of the CMB for the presence of ULVZs (well summarized by

---

[1]Department of Earth, Atmospheric, and Planetary Sciences, Massachusetts Institute of Technology, Cambridge, Massachusetts, USA.
[2]Physics Department, University of Connecticut, Storrs, Connecticut, USA.
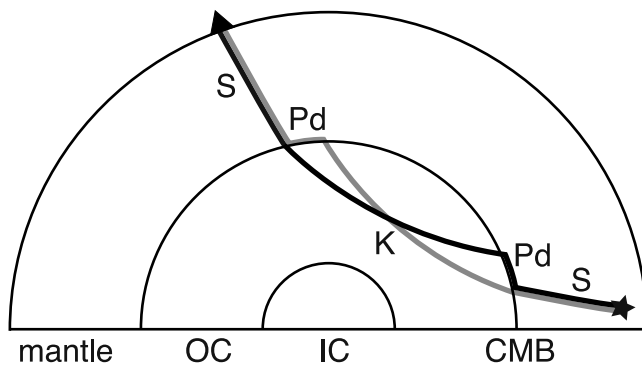
Figure 1. Illustration of the *SPdKS* (thick black line) and *SKPdS* (thick grey line) raypaths with subsegments labeled. *SPdKS* is an *SKS* that intersects the source-side CMB at the *ScP* critical angle and propagates along the mantle side of the CMB as a diffracted *P* wave (*Pd*) for some distance. *SKPdS* is the same phenomenon on the receiver-side CMB. Star shows earthquake source, and triangle shows receiver location. IC, inner core; OC, outer core; and CMB, core-mantle boundary.

Thorne and Garnero [2004]). A phase which has played a particularly important role in the study of ULVZs is *SPdKS*/ *SKPdS* (Figure 1), which is derived from an *SKS* wave intersecting the CMB at the ray parameter for which there is a complex pole in the mantle *S* to core K transmission coefficient. This results in a diffracted *P* wave (P_{diff}, or *Pd*) traveling along the mantle side of the CMB on either the source (*SPdKS*) or receiver (*SKPdS*) side of the path [*Choy*, 1977]. (Henceforth we refer to both the source-side *SPdKS* and the receiver-side *SKPdS* as "*SPdKS*".) Because the mantle and core paths of *SKS* and *SPdKS* are nearly identical, comparison of these two phases allows isolation of travel time and waveform effects of CMB structure. Short- and long-period *SPdKS* have been used to search for and characterize ULVZs on the CMB under the Pacific Ocean, North America, Iceland, Africa, the Atlantic Ocean, and the Indian Ocean [*Garnero et al.*, 1993; *Garnero and Helmberger*, 1995, 1996; *Helmberger et al.*, 1996; *Garnero and Helmberger*, 1998; *Helmberger et al.*, 1998; *Wen and Helmberger*, 1998; *Helmberger et al.*, 2000; *Rondenay and Fischer*, 2003; *Thorne and Garnero*, 2004].

[5] Most previous *SPdKS* studies applied 1-D modeling approaches to characterizing the ULVZ layer. A puzzle, however, is that the best fitting 1-D ULVZ structures for earthquake-station pairs with very similar *SPdKS* CMB paths are often quite different. In section 4.2 we present a case where two *SPdKS* paths are separated by less than 50 km and yet one is best modeled by PREM and the other by fairly strong velocity perturbations [*Thorne and Garnero*, 2004]. The spatial incoherency of these results may indicate that the assumptions underlying the use of 1-D modeling are not always valid. In addition, 1-D modeling does not exploit the constraints that modern 2-D and 3-D broadband seismic data offer on ULVZ properties such as lateral extent, topography on the upper surface, or lateral variability of seismic velocities and densities within the ULVZ. These 2-D and 3-D properties of ULVZs are

important in understanding the processes that control their formation and their effect on mantle dynamics. For example, laterally broad ULVZs associated with the broad *S* velocity anomalies in the lower mantle would have different geodynamic implications than laterally narrower ULVZs associated with the edges of those lower mantle anomalies where the velocity gradients are strongest [*Thorne et al.*, 2004].

[6] Two notable *SPdKS* studies have modeled the seismic effects of 2-D ULVZ structures. *Helmberger et al.* [1996] modeled *SPdKS* waveforms due to 2-D CMB structure with the Cagniard-de Hoop method by combining different 1-D source and receiver-side CMB structures [see also *Rondenay and Fischer*, 2003]. *Wen and Helmberger* [1998] combined generalized ray theory solutions, finite difference calculations, WKB, and Kirchhoff theory to model wave propagation through a variety of dome and box-shaped 2-D ULVZ structures on the CMB. While both of these studies yielded interesting results, neither constrained the sensitivity of *SPdKS* to the lateral extent of ULVZs, as the *Helmberger et al.* [1996] method assumes quasi 1-D ULVZ structures on each side of the CMB and *Wen and Helmberger* [1998] prescribed a limited range of lateral dimensions.

[7] We introduce a new approach to modeling seismic wave propagation through 2-D ULVZ models, the pseudospectral method [*Fornberg*, 1988, 1996; *Furumura et al.*, 1998; *Cormier*, 2000], which combines the flexibility of arbitrarily complex velocity structures with the simplicity of a single numerical approach. We focus on two main points of inquiry. First, how does the sensitivity of the *SPdKS* phase to a 2-D ULVZ centered on the P_{diff} inception point depend on the lateral extent of the ULVZ? Second, how sensitive is *SPdKS* to finite lateral extent of ULVZs that are offset from the P_{diff} inception point but still within the P_{diff} propagation path along the CMB?

2. Forward Modeling

2.1. Pseudospectral Wave Propagation

[8] Global seismic wave propagation through 1-D and 2-D ULVZs is modeled using a cylindrical pseudospectral algorithm [*Cormier*, 2000; *Van Ark*, 2007]. The pseudospectral method is distinguished by its use of Fourier transforms to estimate the spatial derivatives in the elastic equations and the equations of motion as the wavefield is stepped forward through time. It can be thought of as the highest-order limit of the finite difference method, and is advantageous because this approach results in very low numerical dispersion [*Fornberg*, 1988; *Kosloff and Kessler*, 1990; *Fornberg*, 1996; *Furumura et al.*, 1998; *Cormier*, 2000].

[9] A Gaussian source time function with a width at half height of 0.6 seconds is added to the horizontal (radial) component of the velocity at the source node, 500 km below the surface of the Earth. This source time function corresponds to a source amplitude spectrum of $e^{-0.18\omega^2}$. This source spectrum is relatively white over a broad frequency band, decaying from a peak of 1 at 0 Hz to 0.64 at 0.25 Hz, the passband in which the *SPdKS* phases are commonly observed and studied. We use a horizontal grid spacing of 0.088°, which translates to 10.8 km at the top of the model space, 9.5 km at the surface of the Earth, and 5.2 km at the CMB. The vertical grid spacing is variable [*Fornberg*, 1988; *Tessmer et al.*, 1992; *Nielsen et al.*, 1994; *Furumura et al.*,
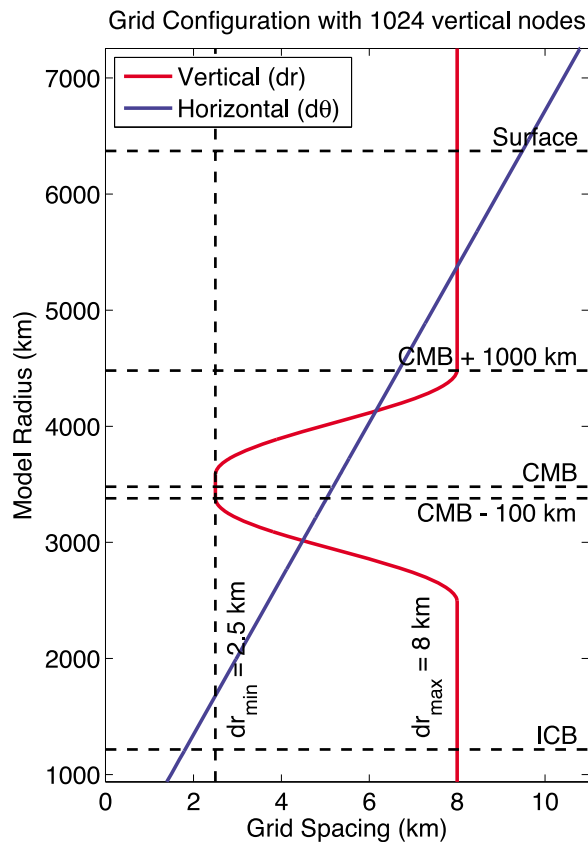
Figure 2. Radial Δr and lateral $\Delta \theta$ grid node spacing as a function of model radius. Minimum radial grid spacing of 2.5 km is maintained for 100 km above and below the CMB and then gradually increased with a cosine shape to 8 km for the rest of the grid. Lateral grid spacing is constant in angular measurement and therefore varies linearly in kilometers as a function of radius.

1998], with 8 km spacing for most of the mantle and core, 2.5 km spacing for a region extending 100 km above and below the CMB, and a gradual transition between the two regimes (Figure 2). Options are included to incorporate viscoelastic attenuation by superposing memory functions [*Robertsson et al.*, 1994; *Blanch et al.*, 1995] to simulate a near constant attenuation in a broad frequency band. We use a time step of 0.025 s and run the wave propagation simulation for 1640 s. Seismograms are saved by reading out the velocity wavefields at given surface nodes ("receivers") every 0.2 s. A line source to point source correction [*Vidale et al.*, 1985] is applied to correct the pulse shapes of the 2-D simulation to those for a vector point source in three dimensions. The output of radial particle velocity from a staggered-grid/velocity-stress time integration scheme is converted to particle displacement.

[10] This 2-D numerical modeling technique has previously been compared against a 2-D approximate modified WKBJ method [*Ni et al.*, 2003], with slight mismatches understood by differences in model parameterizations and the effects of asymptotic approximations of the 2-D modified WKBJ method. Here, we compare pseudospectral record sections for the radial component of motion in 1-D PREM

(Figures 3a and 3b) against a record section obtained with the asymptotically approximate 1-D full wave method of *Cormier and Richards* [1988] (Figures 3c). Much of the coda in the pseudospectral record section without attenuation (Figure 3a) consists of upper mantle phases *sPPP*, *pPPP*, and *S* to *P* conversions at upper mantle discontinuities. These phases are particularly well excited in this distance range for our choice of source depth and source radiation pattern, producing strong, totally reflected *P* waves at near grazing incidence to the 400 and 670 km discontinuities of PREM at range intervals where the multiple *P* legs travel between 20° and 30°. These surface reflected *P* waves can be artificially suppressed in the pseudospectral method by assuming strong upper mantle *P* attenuation (Figure 3b). In 1-D modeling codes (e.g., Figure 3c), these *P* wave surface reflections are commonly ignored by options that omit surface interactions. Omitting attenuation with our choice of source depth and source radiation pattern may overestimate the effects of interfering multiple *P* waves, but we chose to turn off attenuation in most of our modeling runs to increase the frequency content of the *S* waves to better resolve the interference of closely spaced *SKS* and *SPdKS* arrivals.

[11] All synthetic record sections contain the effects of inner core structure in the *SKIKP* + *SKIIKP* + .. + *SKiKP* phase branches, which cross the *SPdKS* phase near 124° for a source at 500 km depth. Its perturbation of the *SPdKS* is small, in agreement with modeling results shown by *Thorne and Garnero* [2004], but must be carefully considered in interpreting complexity of the *SPdKS* displacement waveform in the range surrounding the travel time crossing.

[12] A notable difference between the numerical method (Figures 3a and 3b) and the asymptotically approximate method (Figure 3c) is a more rapid decay with distance of the *SKS* phase in the latter. This is due to the inclusion of 3-D geometric spreading in the asymptotically approximate method but not in the numerical method. The 2-D to 3-D correction in the numerical method only includes the 3-D frequency and phase corrections. The 3-D spreading correction can be applied to individual phases in the numerical method by multiplying amplitudes by $\sqrt{p/\sin(\Delta)}$. This is simple to apply to phases characterized by energy concentrated in a narrow range of horizontal slowness, p, but impractical to include across the entire time length of a seismogram, which may consist of many phases having different slownesses. When this spreading correction is applied to individual phases synthesized by the numerical method and compared to the individual phases synthesized by the asymptotically approximate method, the waveforms can be overlain without mismatch to within the accuracy of trace line widths[*Van Ark*, 2007].

[13] Other differences that can be seen between the numerical method and the approximate method are due to differences in the frequency content and waveform shapes of diffracted phases. These differences are just perceptible in the *SPdKS* phase at shorter range but especially apparent in the diffraction from the *sSKP* caustic. For diffracted phases, the predictions from the numerical method can be expected to be more reliable than those of the high-frequency method, which will tend to accumulate greater error as the diffracted phases become more enriched in lower frequency.
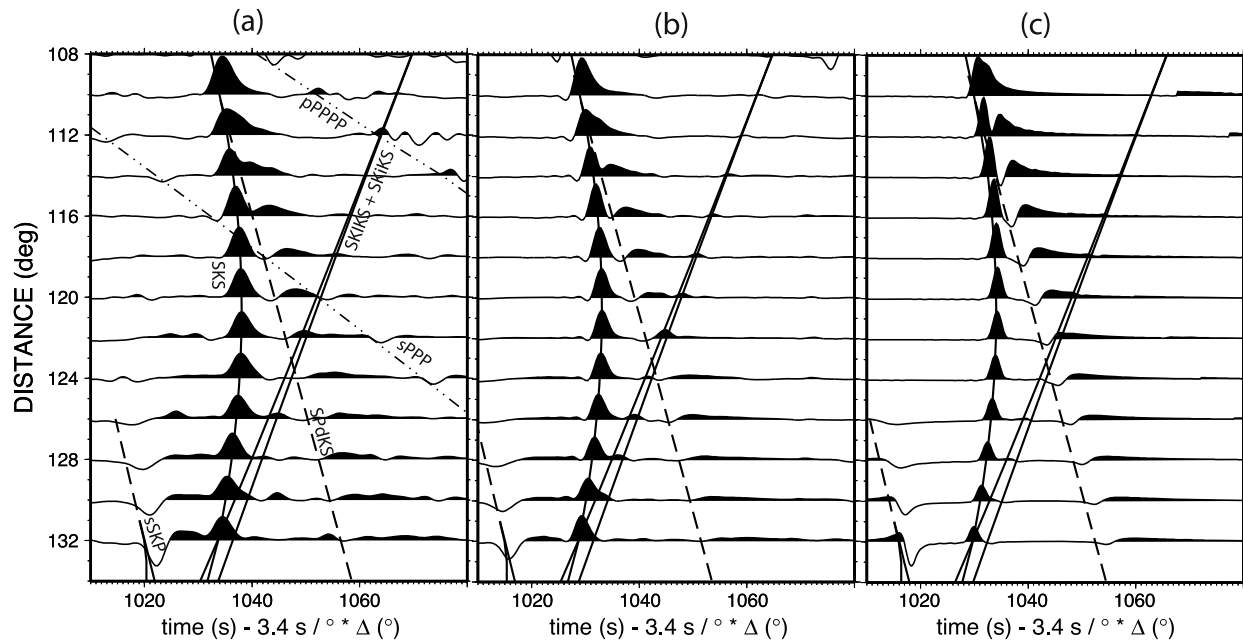
Figure 3. Radial component of displacement synthesized for a radial vector point source at 500 km depth using (a) the pseudospectral method with no Earth attenuation, (b) the pseudospectral method with no *S* attenuation but the *P* attenuation model of PREM doubled, and (c) the asymptotically approximate full wave method of *Cormier and Richards* [1988] with no attenuation. PREM predicted ray theoretical travel times of *SKS* and *SKIKS* + *SKIIKS* + … + *SKiKS* are shown by solid lines; predicted earliest arrival times of diffracted *SPdKS* and the caustic diffraction of *sSKP* are shown by dashed lines; and sPPP and *pPPP* are shown by dash-dotted lines.

2.2. *SPdKS* Measurement

[14] We use the *SPdKS*-*SKS* delay time as the main parameter for characterizing ULVZ structure. While differences in *SKS* and *SPdKS* waveform shape and amplitude are also of interest, they are more difficult to quantify and are complicated in our synthetic seismograms by the presence of upper mantle multiple phases (*sPPP*, *pPPP*, *PPPP*, etc.) that interfere with the *SKS* and *SPdKS* arrivals in the epicentral distance range of interest. In addition to the *SPdKS*-*SKS* differential time, the epicentral distance at which *SPdKS* first appears in the synthetic seismograms and the absolute moveout of the *SPdKS* phase are also useful for characterizing ULVZ velocities, but these parameters are less readily observable on seismograms from single stations or arrays that are not aligned along the event-station great circle path. Referencing the *SPdKS* travel times to the *SKS* travel times removes most of the influence of source parameters and the mantle and core portions of the wave propagation path and allows us to focus on the influence of the CMB portion of the *SPdKS* path.

[15] In order to more quantitatively compare the *SPdKS* arrivals resulting from different velocity models, we use the following processing steps. First, the *SKS* arrivals are automatically picked, starting with the *SKS* predicted travel time from the TauP toolkit [*Crotwell et al.*, 1999] and finding the appropriate zero crossing near that prediction. Second, *SPdKS* arrival times are hand picked on each section of epicentral distances between 104° and 131° and the difference between *SPdKS* travel times for each ULVZ model and *SPdKS* travel times for PREM are calculated.

This relative *SPdKS* delay is approximately constant over the epicentral distance range of interest, so we also calculate the mean *SPdKS* travel time delay relative to PREM for a given ULVZ model by averaging over all epicentral distances for which *SPdKS* is observed in the synthetic seismograms.

2.3. P_{diff} Inception Point Locations

[16] In order to create 2-D ULVZ velocity models to explore the properties of *SPdKS*, we need to understand where the P_{diff} inception is expected to occur on the CMB. As *Choy* [1977] described and *Garnero et al.* [1993] and *Helmberger et al.* [1996] elaborated upon, there is a particular ray parameter, p_{incep}, for which a complex pole exists in the mantle *S* to core *K* transmission coefficients and *S* wave energy incident on the CMB is converted to a diffracted *P* wave traveling along the mantle side of the core-mantle boundary. The *SPdKS* inception slowness for a given velocity model is calculated with the simple formula $p_{incep} = R_{CMB}/V_P$ where V_P is the *P* wave velocity on the mantle side of the CMB. This parameter has values ranging from 253.7 s/rad (4.43 s/°) for PREM to 281.9 s/rad (4.92 s/°) for a 10% *P* wave velocity reduction at the base of the mantle.

[17] We use ray tracing as implemented in the TauP Toolkit [*Crotwell et al.*, 1999] to calculate the location of the critical point of P_{diff} inception along the *SPd*(iff)*KS* and *SKPd*(iff)*S* paths for a suite of one-dimensional ULVZ and PREM velocity models. This calculation finds the location at which an *SKS* ray of the inception slowness p_{incep} pierces the source and receiver sides of the CMB for a given velocity model. We also find the epicentral distance at
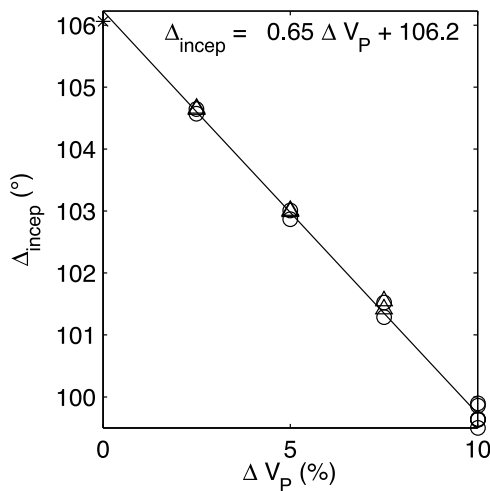
Figure 4. P_{diff} inception distance versus P velocity perturbation at the base of the mantle. Δ_{incep}, epicentral distance for the inception of P_{diff} segments of $SPdKS$ waves. ΔV_P, P velocity perturbation at the base of the mantle for PREM (star) and 1-D ULVZ models with thicknesses between 5 and 40 km, ΔV_P between 2.5 and 10%, and $\Delta V_P{:}\Delta V_S$ velocity ratios of 1:1 (triangles) and 1:3 (circles). Calculated values of Δ_{incep} are ray theoretically based.

which the SKS ray with slowness p_{incep} reaches the receiver and label this the inception distance, Δ_{incep}. This is the epicentral distance at which the SKS and $SPdKS$ travel time curves diverge. The length of the P_{diff} segment along the CMB within the $SPdKS$ path is the difference between the epicentral distance at which the $SPdKS$ phase is observed and Δ_{incep}.

[18] In theory, two factors control the position of the P_{diff} inception point along the SKS raypath and the corresponding Δ_{incep} at which the $SPdKS$ phase is first observed. The mantle-side P wave velocity at the CMB controls the inception slowness directly. Then the integrated effect of (1) the height of the velocity anomaly and (2) the magnitude of the S velocity perturbations controls the amount of deflection the mantle S wave experiences in the ULVZ and therefore the location at which the ray path for a given inception slowness pierces the CMB and reaches the receiver. Figure 4 shows the ray theoretically based $SPdKS$ inception distance for a suite of 1-D CMB models that range from PREM to ULVZs of thicknesses between 5 and 40 km, P velocity variations between 2.5 and 10%, and $P{:}S$ velocity perturbations ratios of 1:1 and 1:3. It is clear that the P velocity at the base of the mantle is the dominant factor influencing the epicentral distance at which $SPdKS$ should first be observed and the location of the corresponding P_{diff} inception points.

[19] These results imply that if it were possible to trace back the $SPdKS$ signal and determine the inception epicentral distance using array data covering a useful range of epicentral distances (95°–130°), it would provide an independent constraint on the P velocity perturbation at the base of the mantle. This scenario may be less precise when applied to real, finite frequency waves for which the single inception point of ray theory becomes an inception region representing the intersection of the core-mantle boundary with a frequency-dependent sensitivity volume surrounding the S ray.

2.4. Ultralow-Velocity Zone Models

[20] All velocity, density, and attenuation Earth models (henceforth referred to as simply "velocity models") presented in this paper are based on the one-dimensional isotropic Preliminary Earth Reference Model (PREM) [*Dziewonski and Anderson*, 1981]. The crust and ocean layers of PREM, however, are replaced by mantle parameters. These low-velocity regions occur in the portion of the grid space with the greatest lateral grid spacing and therefore would limit the frequency content needed for high accuracy. Because the SKS and $SPdKS$ paths through the crust and mantle are nearly identical, this substitution maximizes the possible frequency content of our results with no negative effects on our ability to study the sensitivity of these seismic waves to CMB structure.

[21] "Ultralow-velocity zones" (ULVZs) are created by multiplying the 1-D PREM P and S wave velocities by a 2-D distribution of perturbation factors in the region of interest just above the CMB. Table 1 summarizes the parameters varied in the 91 different ULVZ models we ran with the pseudospectral code. All used $P{:}S$ velocity perturbation ratios of 1:3 as suggested by *Williams and Garnero* [1996] for core-mantle boundary velocity reductions related to the presence of partial melt. Although some interpretations imply that ULVZs are also associated with positive density anomalies (e.g., iron enrichment), we limit our discussion to the effects of velocity perturbations. The validity of this strategy is supported by a modeling exercise showing that density perturbations do not affect the characteristics of the SKS and $SPdKS$ waveforms that are analyzed in this study (see Figures S1–S3 in the auxiliary material).[1]

[22] Four classes of ULVZ models were run. First, 10 one-dimensional models were run. PREM is used as a baseline for comparing the synthetic seismograms produced by all other models. The other nine (Figure 5a) contain ULVZs of varying thicknesses, varying velocity perturbations, and in two cases, varying vertical gradients in velocity perturbation at the top of the model.

[23] If ULVZs are the result of partial melting or some other interaction between the geotherm and the chemical composition of the lower mantle rocks, we might expect the ULVZ upper boundary to be gradational. In contrast, if ULVZs are related to a phase change over a fairly small pressure (and therefore, depth) range, similar to the upper mantle discontinuities, a much sharper ULVZ upper boundary might be expected. We test whether SKS and $SPdKS$ waveforms would be sensitive to the difference between sharp and gradational ULVZ upper boundaries using two models with vertical gradients in ULVZ velocity perturbations (Table 1).

[24] The second class of velocity models (Figures 5b and 5c) feature a simple ULVZ with constant velocity perturbations on either the source or the receiver side of the core mantle boundary region. The CMB region on the other side of the SKS raypath has PREM velocities. A smooth cosine horizontal gradient transitions between the ULVZ velocity per-

Table 1. ULVZ Models[a]

| Model Group	Location	Length	Lat Grad	Thickness (km)	ΔV_P (%)
1-D constant (7)	everywhere	180°	—	5, 10, 20[b], 30, 40[b]	5[b], 10
1-D full gradient[c] (1)	everywhere	180°	—		
1-D half gradient[d] (1)	everywhere	180°	—		
1-sided source (7)	source-side	54°	20°	5, 10, 20[b], 30, 40[b]	5[b], 10
1-sided receiver (7)	receiver-side	126°	20°	5, 10, 20[b], 30, 40[b]	5[b], 10
Inception sensitivity (60)	centered on inception point	10, 20, 30, 60, 120, 240, 480, 600, 720, 840, 960, 1920 km[e]	—	5, 10, 20, 30, 40	10
Distal ULVZ sensitivity (4)	centered on core entry point for $\Delta = 121.5°$	13°	0.5°	20, 40	5, 10
Proximal ULVZ sensitivity (4)	begins 2° after Δ_{incep}	6°	0.5°	20, 40	5, 10

[a]Where lateral cosine gradients (Lat Grad) of the full given length are used, ULVZ lengths are measured using the midpoint of the lateral cosine gradient on either side of the ULVZ. Unless noted otherwise, all combinations of the parameters shown were run, for example, each length with each thickness of the Inception Point models. The total number of models in each group is given in parentheses. All models were run with $\Delta V_P:\Delta V_S$ of 1:3.

[b]The 5% models run only for 20 and 40 km thicknesses in 1-D and 1-sided groups.

[c]Linear gradient from 0 ΔV_P 40 km above CMB to 10% ΔV_P at CMB.

[d]Linear gradient from 0 ΔV_P 40 km above CMB to 10% ΔV_P 20 km above CMB, constant 10% ΔV_P down to CMB.

[e]These lengths correspond to approximately 0.16°, 0.33°, 0.5°, 1°, 2°, 4°, 8°, 10°, 12°, 14°, 16°, and 32° at the CMB.
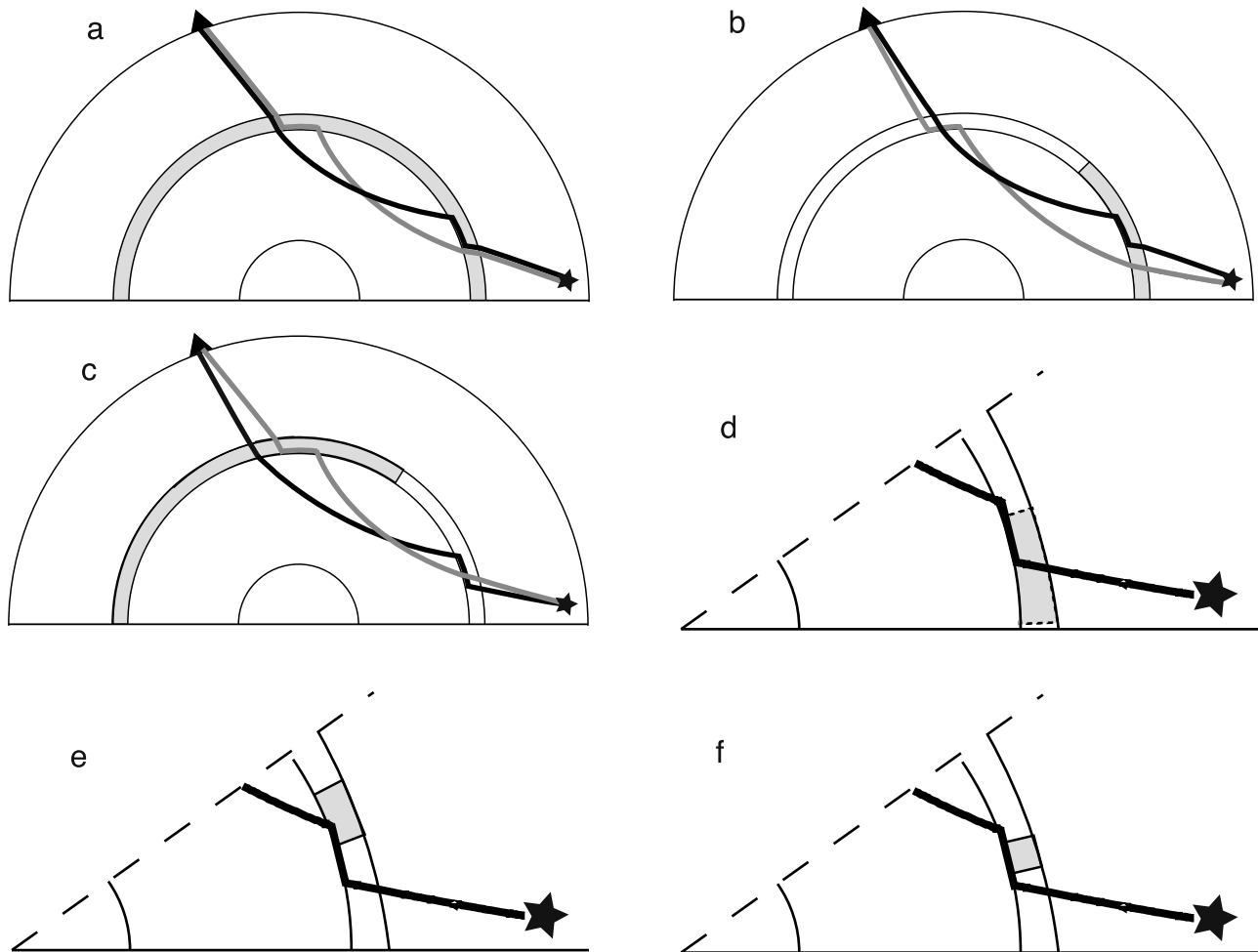
Figure 5. Illustrations of various ultralow-velocity zone model configurations. *SPdKS* and *SKPdS* ray-paths are displayed as black and grey lines, respectively. Light shaded patch shows approximate ULVZ geometry, with exaggerated vertical dimensions. (a) One-dimensional ULVZ models. (b) One-sided ULVZ models, source side. (c) One-sided ULVZ models, receiver side. Zoom in on the interaction between *SPdKS* and the CMB on the source side for (d) finite length ULVZ models, centered on the inception point, (e) finite length ULVZ models, distal, and (f) finite length ULVZ models, proximal.

turbations and the PREM velocity model halfway between the source and the receivers. These represent the simplest possible 2-D ULVZ models and also form a useful comparison set for narrower finite length 2-D models described below.

[25] The third class of velocity models is designed to explore how long a simple, finite length ULVZ centered on the P_{diff} inception point must be to produce detectable effects on the *SPdKS* arrival times and waveforms (Figure 5d). Each model is centered on the P_{diff} inception point for the equivalent 1-D ULVZ model and has sharp upper boundaries and sharp lateral edges. The use of sharp lateral edges is motivated here by the need to model ULVZs with lengths as short as 10 km and to increase the length by increments of 5 km on both sides of the ULVZ, i.e., changes that would be overly smoothed if lateral gradients of several tens of kilometers were used. As we will see in the results of section 3.3, these sharp boundaries cause only minor reductions in waveform amplitude (perhaps due to scattering attenuation), without modifying the main observations of *SPdKS*-*SKS* delay times used in our analysis.

[26] The fourth class of ULVZs is designed to test the sensitivity of the *SPdKS* phase to different portions of the *P* diffracted segment along the CMB. "Distal" ULVZ models (Figure 5e) are placed well beyond the P_{diff} inception point, such that only *SPdKS* waves recorded at epicentral distances of 115°–128° possess P_{diff} segments that enter the core from the ULVZ. Conversely, "proximal" ULVZ models (Figure 5f) are placed to begin near the P_{diff} inception point (i.e., 2° beyond it), and to possess P_{diff} segments that enter the core from the ULVZ for recording distances between 108° and 114°.

3. Results

3.1. One-Dimensional Modeling Results

[27] Three of the seismogram sections synthesized by the pseudospectral propagation code through PREM, 1-D, and one-sided ultralow-velocity zone models are presented in Figure 6. For the suite of synthetic sections produced in this study, the phases are identified by ray theoretical modeling of common *SKS*-CMB interactions in the presence of ULVZs (see Figure 7 for a description of the phases identified in Figure 6 and see Figures S1 and S2 for a description of all considered phases). A complete set of seismic sections for all 1-D and one-sided models are presented in Figure S4.

[28] A primary observation from Figures 6b, 6e, and 6h is that very thick, strong ULVZs (in this case, 40 km thick with 10% *P* and 30% *S* velocity reductions) have strong effects on the *SKS* waveform as well as the *SPdKS* arrival time. In this case, the *SKS* phase is split into two main peaks

of quasi-equal amplitude, one of which arrives near the PREM *SKS* travel time and one of which arrives 5–6 s later. This travel time separation is well modeled by an *S* to *P* conversion at the top of the ULVZ on either the source or receiver side (Figures S1 and S2). The second of the "*SKS*" peaks is therefore the true *SKS* and the first peak is a phase we will call *SPKS* (following the naming convention adopted in Figure 6 and in the auxiliary material). Note that *SPKS* is also preceded by a small precursor identified by TauP modeling as *SPKPS*, a wave that travels as *P* in the ULVZ on both the source and receiver sides (Figure 7).

[29] As the strength of the ULVZ decreases with either thinner ULVZs or smaller velocity reductions (Figure S4) the travel time separation between *SPKS* and *SKS* narrows and the *SKS* pulse returns to a very PREM-like shape and arrival time. *Stutzmann et al.* [2000] predicted *SPKS–SKS* travel time separations of 3.6 s, 2.3 s, and 1.3 s for 10% *P* and 30% *S* velocity perturbations in layers of 30, 20, and 10 km thickness, which agrees well with our results. They used the lack of observed *SKS* precursors in a data set with *SPdKS* paths sampling the southwest Pacific CMB to place upper limits on the possible ULVZ strength in that region.

[30] It is clear from a comparison of the mean *SPdKS* delays that very similar results are produced for the ULVZ models with equivalent integrated vertical velocity profiles (see Figure S4). Thus the *SPdKS* delays are almost identical for the following sets of models: the 40 km thick constant ULVZ with 5% ΔV_P, the 20 km thick constant ULVZ with 10% ΔV_P, and the "full gradient" 40 km thick ULVZ; the 20 km thick constant ULVZ with 5% ΔV_P and the 10 km thick constant ULVZ with 10% ΔV_P; and the 30 km thick constant ULVZ with 10% ΔV_P and the "half gradient" ULVZ. These similarities in mean *SPdKS* delays between different models point to two aspects of the nonuniqueness of ULVZ modeling. First, there is a clear tradeoff between ULVZ layer thickness and velocity perturbations. This result agrees with, and provides independent support for, similar observations from previous studies [*Helmberger et al.*, 1996; *Garnero and Helmberger*, 1998; *Garnero et al.*, 1998; *Garnero and Jeanloz*, 2000a]. Second, there is also nonuniqueness with respect to vertical variations in ULVZ properties.

[31] The *SPdKS* traveltime delay due to a linear gradient in velocity perturbations over thickness *h* appears equivalent to that of a simple homogeneous layer with a sharp upper boundary and the full velocity perturbation over thickness *h*/2. At the wavelengths under consideration for *SKS* and *SPdKS* here, the travel times are sensitive to the average vertical properties of the ULVZ and are largely insensitive to details of the vertical velocity structure. There are slight differences between the *SKS* and *SPdKS* waveforms pro-

Figure 6. Pseudospectral *SV* displacement seismograms for three categories of CMB velocity models. (left) PREM [*Dziewonski and Anderson*, 1981]. (middle) A 40 km thick, 1-D ULVZ with 10% *P* and 30% *S* velocity reduction (Figure 5a). (right) A 40 km thick, source-side ULVZ with 10% *P* and 30% *S* velocity reduction (Figure 5b). (a–c) The raw seismogram sections. (d–f) Seismogram sections with phases predicted by TauP modeling (see Figure 7 and Figures S1 and S2). Yellow dashed line indicates predicted arrival times for *sPPP*, *PPPP*, *pPPP*, and other multiple *P* arrivals (see Figure 3). Observed phases related to *SKS* and its interactions with the CMB are listed in the legends. (g–i) Manual picks used for the purpose of this study. The reference phase, $SPdKS_{PREM}$, is picked on Figure 6g. For 1-D models, the relative delay time corresponds to $SPdKS_{1D}$-$SPdKS_{PREM}$ (Figure 6h). For 2-D ULVZ models, the relative delay time corresponds to $SPdKS_{2D-U}$-$SPdKS_{PREM}$ (Figure 6h), where $SPdKS_{2D-U}$ is the phase that possesses a *Pd* segment in the one-sided ULVZ (see Figure 7).
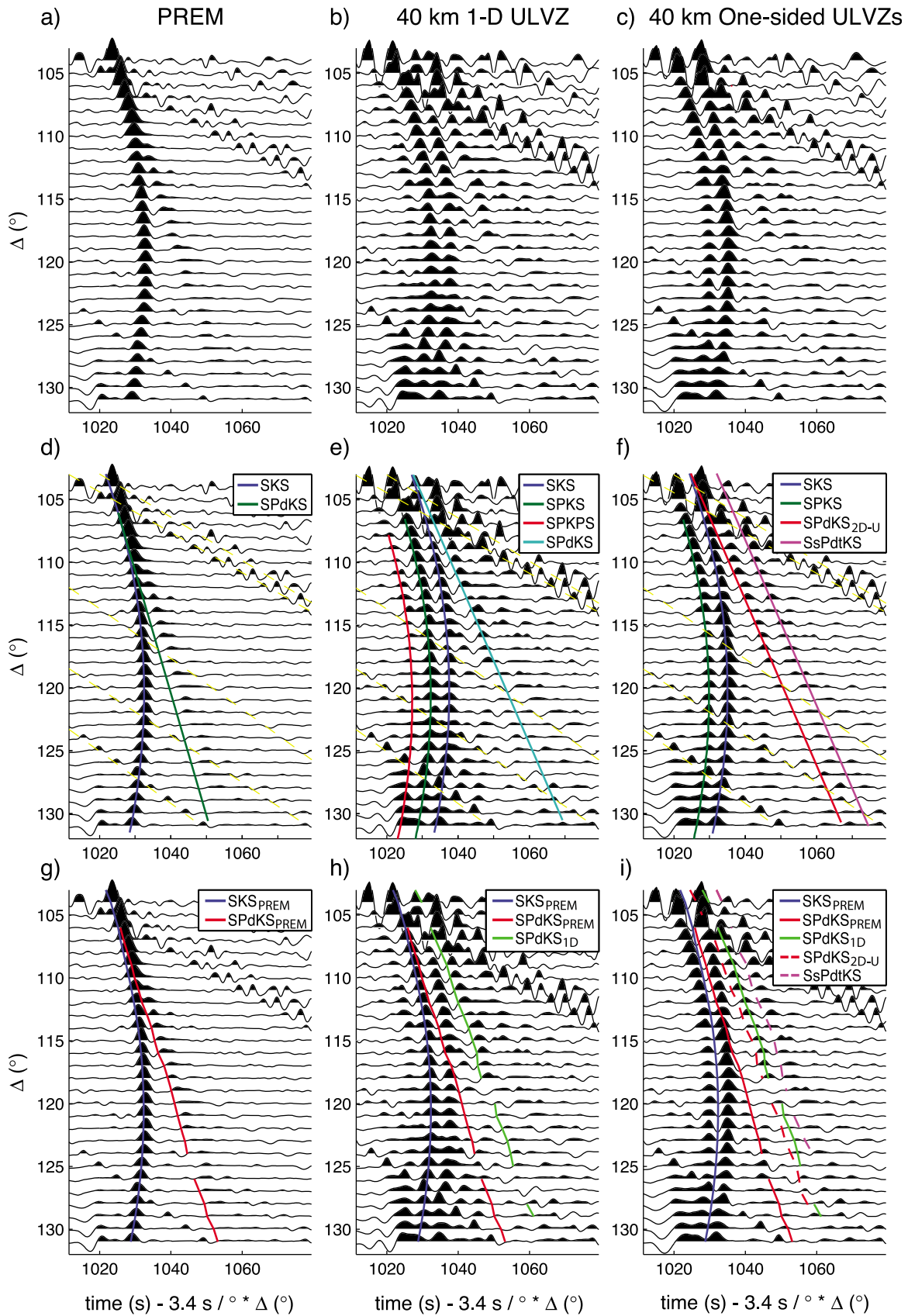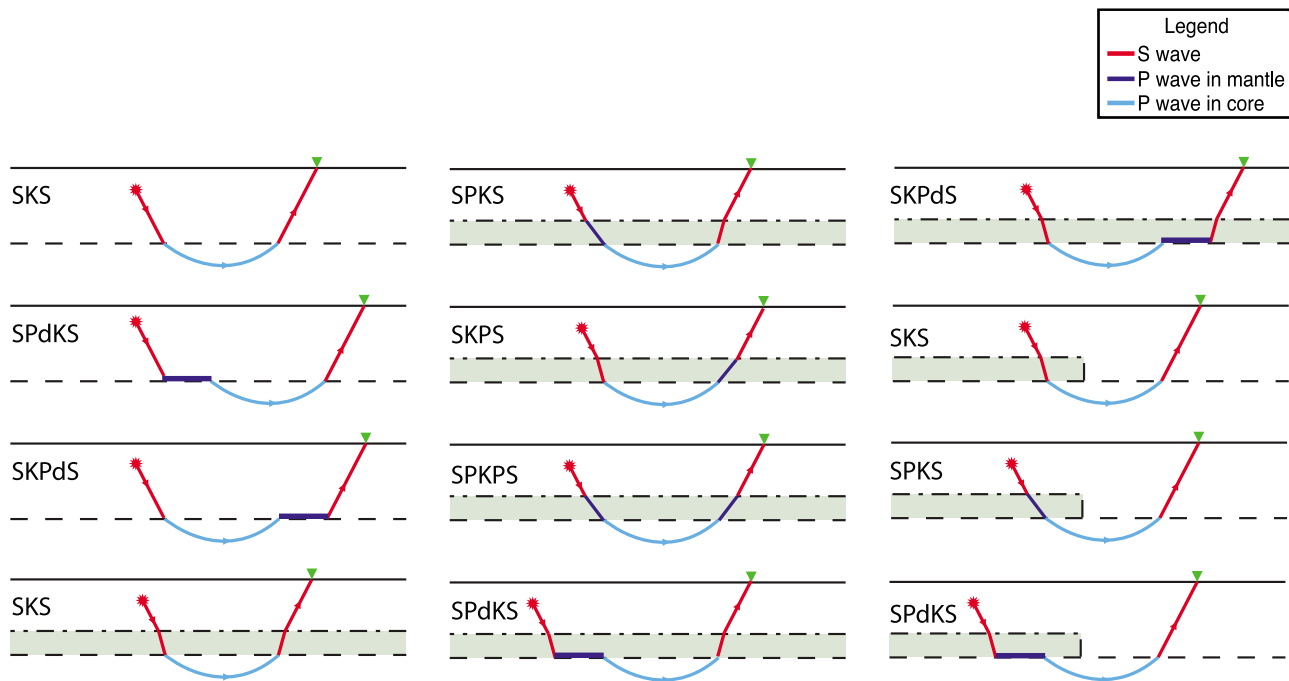
RONDENAY ET AL.: SEISMIC MODELING OF 2-D ULVZS

Figure 6

Figure 7. Phase nomenclature and corresponding schematic ray theoretical representation. The solid line denotes the surface, the dashed line denotes the CMB, grey bands represent ULVZs, and the dash-dotted line denotes the top of the ULVZs. Raypaths from the source (asterisk) to the station (triangle) comprise distinct elements of *S* waves and *P* waves (see legend).

duced with sharp versus gradational upper boundaries; however, they are not detectable using the *SPdKS* travel time delay metric that we use here. For this reason, the rest of the models presented here have simple vertical velocity profiles corresponding to constant velocity perturbations on PREM.

[32] We parameterize the ULVZ strength as the product of the ULVZ effective thickness, *h* (km), and the *P* velocity perturbation at the base of the ULVZ, ΔV_P (%). Figure 8 shows the linear least squares fit of the *SPdKS* delays relative to PREM, dt, and their corresponding ULVZ strength for our 1-D models. This reduction of 10 seismic sections to 9 mean *SPdKS* relative delay times and then to 2 polynomial parameters suggests the ability to constrain some combination of ULVZ properties from the *SPdKS* travel time delays. If our $h\Delta V_P$ parameterization of ULVZ strength captured all the relevant ULVZ properties, we would expect the intercept of the $dt = f(h\Delta V_P)$ equation to be zero. As our fit is instead $dt = 0.02 \ h\Delta V_P + 0.58$, it suggests that 0.58 s of *SPdKS* delay is unaccounted for in our current parameterization. The source of this 0.58 second delay is the result of complex phase shift in the *SPdKS* waveform affecting the travel time pick from the apparent first break.

3.2. One-Sided ULVZ Results

[33] We model seismic wave propagation through ULVZ models that perturbed the velocities on either the source or the receiver side of the CMB (Figures 5b and 5c). However, we plot only the source-side synthetic seismogram in Figures 6c, 6f, and 6i as they are identical to the receiver-side synthetic seismogram. This ambiguity between *SPdKS* signals due to source and receiver side CMB velocity

structure is well discussed by *Garnero and Helmberger* [1995], who point out that the "*SPdKS*" phase is actually the combination of an infinite set of raypaths that sample both sides of the CMB in various proportions; the *SPdKS*
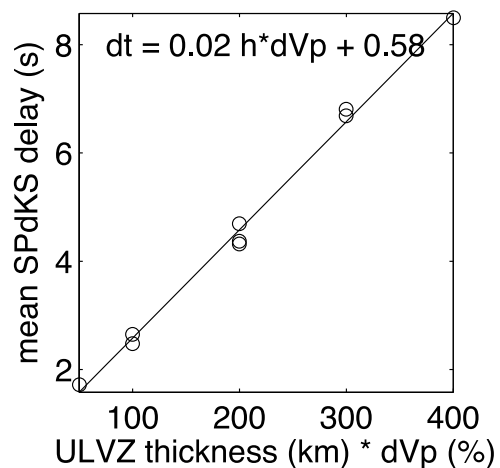
Figure 8. Relationship between ULVZ strength and the mean *SPdKS* delay relative to the *SPdKS* travel time in PREM, *dt*. The ULVZ strength is parameterized as the thickness of the ULVZ, *h*, times the *P* velocity perturbation at the base of the ULVZ, ΔV_P. For the 40 km thick "full gradient" model the effective thickness is taken to be 20 km. For the 40 km thick "half gradient" model, the effective thickness is taken to be 30 km. Circles show mean *SPdKS* delays for all 1-D ULVZ models, and line shows the linear fit to those points given by the equation for *dt*.
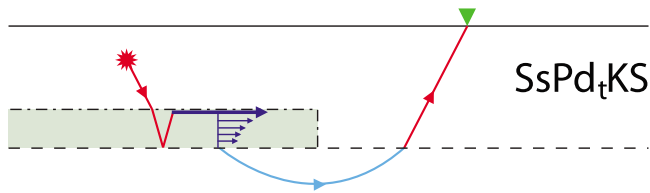
$SsPd_tKS$

Figure 9. Schematic representation of the $SsPd_tKS$ phase, a potential candidate for the secondary pulse observed in the wake of $SPdKS$ in trace sections constructed for one-sided ULVZs. Discontinuities and ray segments are defined as in Figure 7. The $SsPd_tKS$ phase comprises an incident S wave (S) that is reflected off the CMB as an S wave (s) and then converted into a P_{diff} segment at the top boundary of the ULVZ (Pd_t). This Pd_t segment is an evanescent wave with an associated displacement that decays exponentially away from the interface (see parallel blue arrows). At wavelengths of the same order as ULVZ thicknesses or longer (frequencies <1–2 Hz), some of that Pd_t displacement energy reaches the CMB and thus generates a P wave that travels into the outer core and resurfaces on the source-side as an S wave (KS). The $SsPd_tKS$ possesses a ray parameter that is nearly identical to that of $SPdKS$ and trails the $SPdKS$ with a delay corresponding to [ULVZ thickness] × [S wave velocity] consistent with delays observed in Figure 6 and Figures S2 and S4.

and $SKPdS$ rays pictured in Figure 1 that sample only the source or the receiver side of the CMB are end-members of a spectrum of raypaths that contribute to the observed $SPdKS$ signal on a seismic trace.

[34] We find that the 1-D and one-sided $SPdKS$ travel times for thin ULVZs are the same within picking errors (~0.5 s), while still being measurably slower than the PREM $SPdKS$ travel times (~1–3 s). For the strongest ULVZ we model (40 km thick with 10% P and 30% S velocity perturbations), we observe two important differences between the 1-D and one-sided ULVZ models (Figure 6b, 6c, 6e, 6f, 6h, and 6i). First, the one-sided ULVZ models have two distinct arrivals with $SPdKS$ moveout (dashed lines in Figure 6i), while the 1-D ULVZ model has only one clear $SPdKS$ arrival (green line in Figure 6h). Second, the $SPKS$/ SKS amplitude ratio is lower for the one-sided ULVZ models than for the 1-D ULVZ model.

[35] Two $SPdKS$ pulses are expected for a model with two different CMB velocity structures on the $SPdKS$/$SKPdS$ path with different expected ray parameters for P_{diff} inception [*Helmberger et al.*, 1996]. Since one of those two CMB velocity structures is PREM, it is also expected that one of the $SPdKS$ arrivals in the one-sided synthetics would correspond to that modeled for PREM, which is not the case (see Figure S4). Instead, we find that the first one-sided ULVZ $SPdKS$ pulse corresponds to that of a P_{diff} segment traveling on the ULVZ side of the path, while the second comes in ~12 s after the PREM $SPdKS$ arrival. The second one-sided ULVZ $SPdKS$ arrives ~5.6 s after the first, a travel time delay corresponding exactly to one additional S wave segment in the ULVZ at the same ray parameter. The fact that the two pulses exhibit the same moveout suggests that the second pulse comprises also a P_{diff} segment on the ULVZ side of the path.

[36] Despite conducting a thorough phase identification exercise (see Figures S1 and S2), we did not find a simple ray theoretical phase that could cause the second $SPdKS$ pulse. Therefore, we speculate that it is due to either finite frequency or scattering effects. One such possible finite frequency effect is a phase labeled $SsPd_tKS$, which is depicted schematically in Figure 9. This phase possesses an additional S wave segment in the ULVZ, and a P_{diff} segment that travels along the top boundary of the ULVZ while leaking energy into the outer core to complete a path very similar to that of $SPdKS$. A priori, the proposed phase should also be visible as a secondary pulse in the 1-D ULVZ models, but it is not. This may be the result of destructive interference with ULVZ internal multiples, which have stronger amplitudes in 1-D ULVZ models. Alternatively, the secondary pulse could be caused by scattering effects off the lateral boundary of one-sided ULVZs. This model can explain the fact that the pulse occurs only in 2-D models, but no obvious combination of incident and scattered rays can explain the time delay of the secondary pulse. Based on these observation, we favor a finite frequency effect such as $SsPd_tKS$ as the cause of the secondary pulse, but note that further modeling (including finite frequency sensitivity of SKS at the CMB) will be required to better constrain this phenomenon.

[37] The 20 km thick one-sided ULVZ models result in synthetic seismograms with intermediate properties (Figure S4). Their $SPdKS$ arrival times are similar to those observed for the equivalent 20 km thick 1-D model. They have more complicated SKS waveforms than the 5 and 10 km thick models, but not as distinctly split as the 40 km thick model. Whatever processes cause the SKS split in the very strong ULVZ are probably occurring in this half as strong ULVZ, but are more compressed in travel time and therefore less distinct. These observations further support the hypothesis that a phase such as $SsPd_tKS$ may be responsible for the secondary $SPdKS$ pulse.

3.3. Inception Point Sensitivity

[38] A selection of synthetic seismograms from ULVZ models testing the inception point sensitivity is presented in Figure S5. Here we summarize their results by calculating the mean $SPdKS$ delay relative to PREM $SPdKS$ for all 60 inception point sensitivity models and plotting them in Figure 10. Figure 10 therefore provides constraints on the combination of ULVZ thickness, P velocity perturbation, and length that could cause a given $SPdKS$ delay relative to PREM. This information can be further distilled by plotting the slope of each delay line (i.e., colored lines) as a function of ULVZ length (see Figure 11).

[39] Figures 10 and 11 can be used to infer the sensitivity of $SPdKS$ to ULVZ length. They show that $SPdKS$ travel times have no measurable sensitivity to ULVZs with lengths shorter than ~100 km. In fact, the full waveforms for these short ULVZs are nearly indistinguishable from those synthesized for PREM, regardless of the ULVZ thickness (compare Figures S5a, S5g, S5m, S5s, and S5y with Figure S2a). This holds true despite the use of sharp lateral boundaries for these ULVZ models, implying that sharp boundaries do not bias the results. For progressively larger ULVZ lengths, the $SPdKS$ traveltime delays increase to
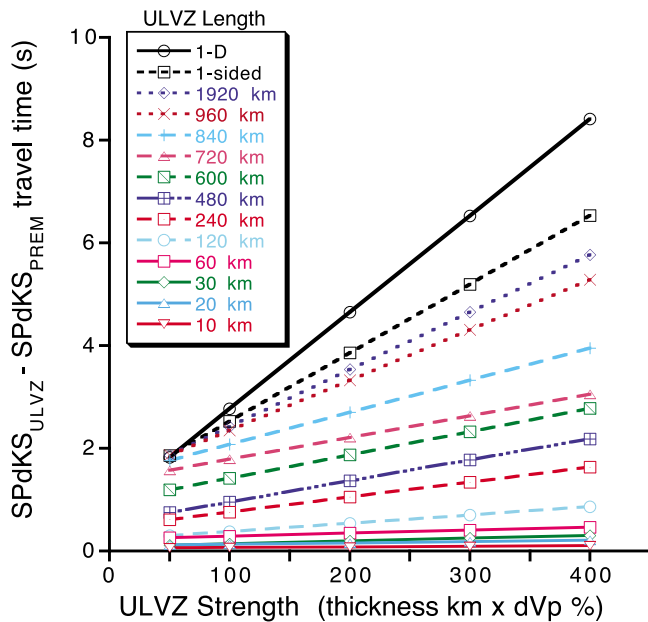
Figure 10. *SPdKS* delay versus ULVZ strength (parameterized as ULVZ thickness multiplied by the ULVZ *P* velocity perturbation) for various ULVZ lengths.

reach asymptotically the delay corresponding to the full one-sided ULVZ.

[40] If we look instead at the waveform variations as a function of ULVZ length, we note that the *SPKS* phase (precursor to *SKS*) observed for the full one-sided ULVZ model becomes apparent only for ULVZ lengths >240 km and that its full amplitude near the *SPdKS* inception distance is attained only for ULVZ lengths >600 km (Figure S5). These values are comparable to published estimates for Fresnel zone dimensions at the CMB for other seismic phases (*PcP* and *ScS*), which are on the order of 200–400 km [*Tkalcic and Romanowicz*, 2002; *Thomas et al.*, 2004; *Braña and Helffrich*, 2004].

[41] Our observations suggest that whereas the sensitivity of *SPKS* can be predicted by Fresnel zone estimates, the same approach may not be applicable to *SPdKS* due to the non-ray-theoretical nature of these phases. However, inferences about the sensitivity of *SPdKS* can be made from the synthetic waveform modeling and, in this respect, our results show that *SPdKS* delays are more sensitive to finite length ULVZs than *SPKS–SKS* waveforms.

3.4. *P*diff Path Sensitivity

[42] The synthetic seismograms modeled in this section test whether the *SPdKS* waveforms are sensitive to velocity structure of the CMB that occurs away from the *P*diff inception point. Complete sets of these seismograms are presented in Figure S6.

[43] *SPdKS* travel times for the distal ULVZ models (Figure 5e) are identical to PREM, and the waveforms look very similar from model to model. The presence of a ULVZ around the area in which the *P* diffracted energy enters the core for a pure *SPdKS* phase (source-side *P*diff component for *SPdKS* recorded at 115°–128°) has no measurable effects on the *SPdKS* arrival in our models.

[44] Representative synthetic seismograms for the proximal ULVZ models (Figure 5f) are shown in Figure 12. Displacing the finite length ULVZ from the inception point to the middle of the *P*diff propagation path (for a recording distance of 116°) results in an intact *SKS* pulse with none of the splitting into *SPKS* and *SKS* that is observed for the 1-D and one-sided ULVZ models presented in sections 3.1 and 3.2. As for the *SPdKS* delays associated with these models, they are generally similar to those observed in the one-sided ULVZ models (compare dashed red line and solid green line in Figure 12). For strong ULVZs, the *SPdKS* phase splits into two pulses: a first weaker one corresponding to *SPdKS*PREM and the second one corresponding to *SPdKS*ULVZ (Figures 12b, S6f, and S6h).

[45] The results presented in this section reflect the fact that *SPdKS* delays are controlled mainly by the velocities sampled by the *P*diff segment traveling along the CMB. In the case of distal ULVZs, the *P*diff segment samples mostly PREM velocities and therefore there is no observable *SPdKS* delay. In the case of proximal ULVZs, the sampled velocities are those of the ULVZ and the delay of the main *SPdKS* pulse is therefore similar to that of an ULVZ model.

4. Discussion

4.1. The 2-D ULVZ Signatures

[46] A summary of the *SKS-SPdKS* waveforms associated with the models ran in this study is presented in Figure 13. Given our modeling results, the following signatures of 2-D ULVZ structures might be found in real seismograms. First, the presence of more than one *SPdKS* moveout event is diagnostic of *SKS* exposure to more than one CMB *P* velocity structure. One-sided ULVZ models with PREM on the other side of the *SPdKS* CMB path can produce two *SPdKS* arrivals with relatively equal amplitude, both delayed relative to PREM. Proximal ULVZs, which describe low-velocity layers located just beyond the *P*diff inception point, result in a low-amplitude *SPdKS* arrival at PREM travel times and a
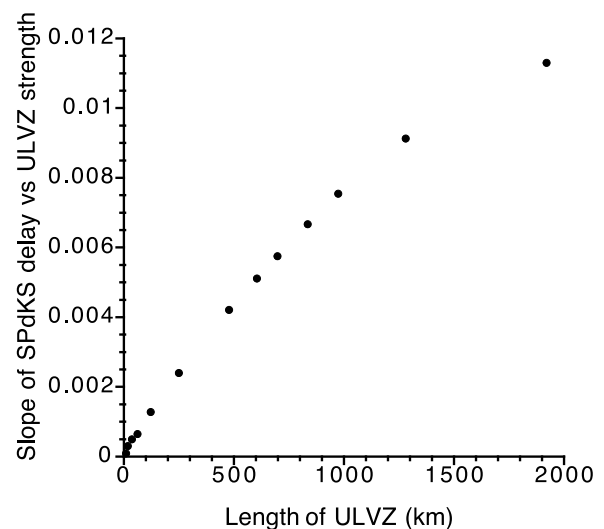
Figure 11. Slopes of 1-D fits to inception model results from Figure 10 versus ULVZ length. This slope is a reasonable proxy for *SPdKS* sensitivity to ULVZs of a given finite length centered on the *P*diff inception point.
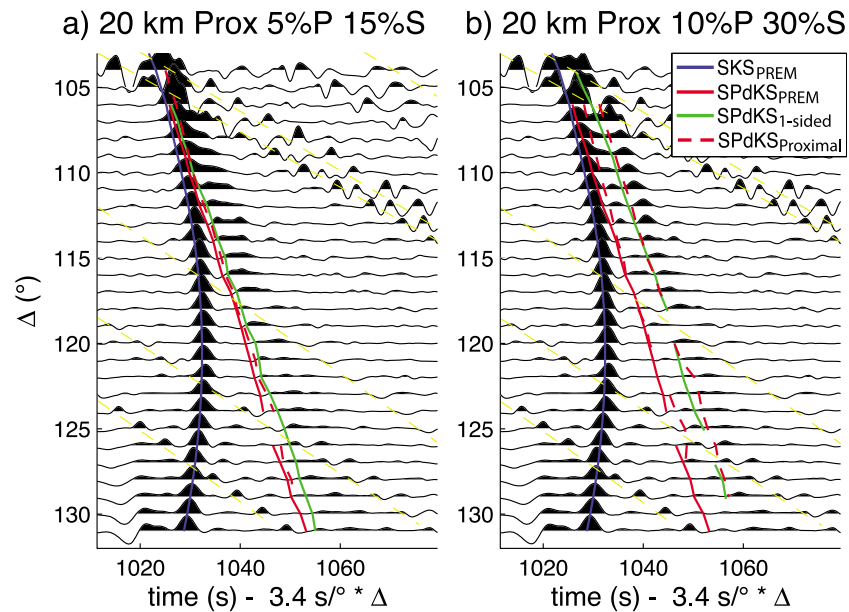
Figure 12. Synthetic seismograms for finite length, proximal ULVZ models (Figure 5f). The thickness of the ULVZ is 20 km, and the velocity perturbations are (a) $5\%V_p$, $15\%V_s$, and (b) $10\%V_p$, $30\%V_s$. Blue line shows *SKS* picks from PREM pseudospectral synthetic seismograms. Solid red line shows PREM *SPdKS* picks. Dashed red line shows *SPdKS* picks for this model. Note that although a partial split of the *SPdKS* is observed in Figure 12a, we do not delineate the second pulse because it is too close to the first pulse and thus is not preceded by a zero crossing (i.e., the reference point for phase picking). Green solid lines show *SPdKS* picks for equivalent one-sided ULVZ model. Yellow dashed lines indicate predicted arrival times for *sPPP*, *PPPP*, *pPPP*, and other multiple *P* arrivals (see Figure 3).

higher-amplitude *SPdKS* arrival at ULVZ travel times. In addition, if the multiple *SPdKS* arrivals can be traced back to their inception epicentral distance, that distance may be used to estimate the *P* velocities at the base of the mantle. However, this estimate is valid only for 1-D or one-sided (full length) ULVZs, since the inception distance is also dependent on the extent of finite length ULVZs (e.g., compare Figures S5y–S5dd).

[47] Second, if an *SPKS* phase is observed, then the relative amplitudes between *SPKS* and *SKS* may be a diagnostic for 1-D versus one-sided ULVZ structure (this quantity can also be modulated by density perturbations, but to a lesser extent; see Figure S3). Such *SKS* precursors, however, have not been commonly observed in previous ULVZ studies. The lack of *SPKS* observations in data might be attributed to gradational, nonsharp ULVZ upper boundaries [e.g., *Rondenay and Fischer*, 2003]. This is consistent with our 1-D ULVZ results, which indicate that vertical gradients in ULVZ velocity perturbations greatly reduce the amplitude of *SKS* precursors while maintaining *SPdKS* delays and moveouts comparable to those associated with ULVZ structure (see Figure S4). Alternatively, the usual absence of large *SPKS* waves may indicate that very strong ($\geq$300 km %) ULVZs are not common at the CMB.

[48] Regarding finite length ULVZs, we do not find any way of distinguishing ULVZs that are strong and short from ULVZs that are weak and long by using only the *SPdKS* travel time delay. The ULVZ length thus becomes another of the parameters in the nonunique ULVZ modeling space that may be traded off against layer thickness, velocity perturbations, and density perturbations. The *SPdKS* travel
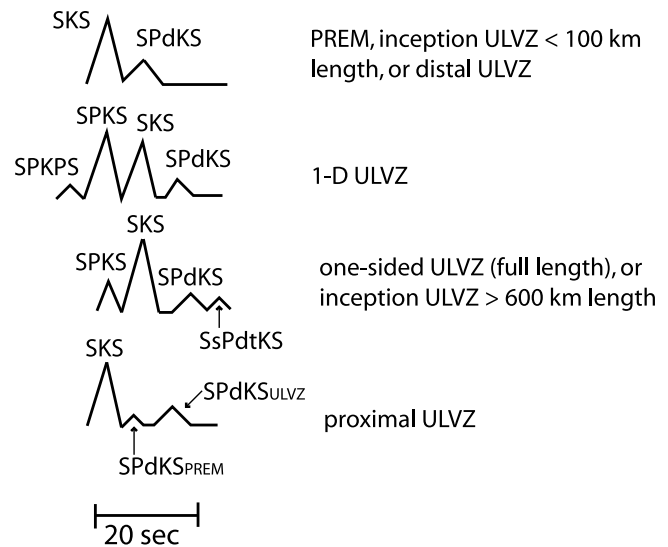
Figure 13. Schematic *SKS-SPdKS* displacement waveforms (*SV* component) for the various synthetic models ran in this study, based on seismograms recorded at 115° epicentral distance. (a) PREM, ULVZs centered on the P_{diff} inception point with ULVZ length <100 km, or distal ULVZ. (b) One-dimensional ULVZs. (c) One-sided ULVZs, or finite length ULVZs centered on the P_{diff} inception point with ULVZ length >600 km and ULVZ strength >200 km %. For shorter lengths and weaker strengths, these phases still exist, but they may not be distinguishable because phase pairs *SPKS-SKS* and *SPdKS-SsPd$_t$KS* are joined in the frequency range considered here. (d) Proximal ULVZ.
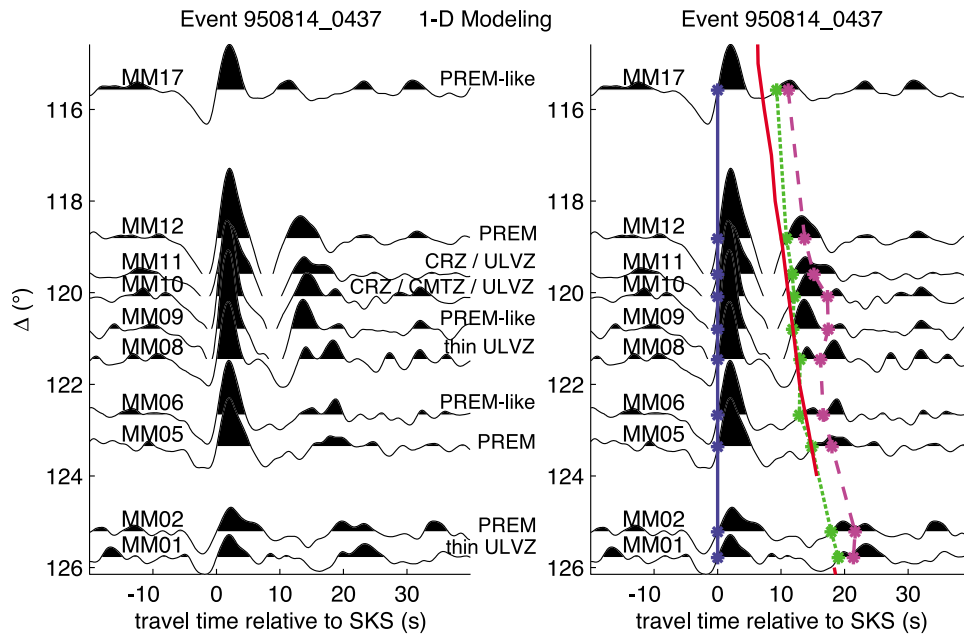
Figure 14. Data section for 14 August 1995 earthquake with a moment magnitude of 6.3 and a depth of 126 km, located near Papua New Guinea and recorded at 10 stations in the MoMa array [*Thorne and Garnero*, 2004]. (left) Data aligned on *SKS* picks, labeled with best fitting 1-D CMB region model(s) for each individual trace [*Thorne and Garnero*, 2004]. ULVZ, ultralow-velocity zone; CRZ, core rigidity zone (small finite rigidity at top of outer core); CMTZ, core-mantle transition zone (linear gradient between lower mantle properties and upper outer core properties). PREM-like results indicates that the best fitting models are PREM and thin (≤ 10 km) "ULVZs" with density perturbations but no velocity perturbations. (right) Same data but with *SKS* picks (solid blue), *SPdKS* picks (dotted green and dashed magenta), and PREM predicted *SPdKS* relative to observed *SKS* arrivals (solid red).

time delay, however, does impose constraints on the minimum combinations of ULVZ strength and length that are required, and these constraints are more restrictive for larger *SPdKS* travel time delays. At the very least, any observable *SPdKS* delay indicates a ULVZ length ≥ 100 km.

4.2. Data and the Real Earth

[49] We look for these 2-D ULVZ signatures in the extensive collection of *SPdKS* seismograms made available online (http://ulvz.asu.edu/) by *Thorne and Garnero* [2004]. Because our synthetic seismometers are linear arrays implicitly aligned with the event-station great circle paths, the series of 10 seismograms presented in Figure 14 is a good subset of the *Thorne and Garnero* [2004] data for comparison with our results. The earthquake source is a 14 August 1995 event with a moment magnitude of 6.3 and a depth of 126 km, located near Papua New Guinea. The event was recorded at 10 stations in the Missouri to Massachusetts (MoMa) linear array [*Wysession et al.*, 1996] with epicentral distances between 115.6° and 125.8°.

[50] Figure 15a shows the expected source-side and receiver-side P_{diff} portions of the *SPdKS* paths for the traces in Figure 14, overlaid on a lower mantle slice from a 3-D global *S* velocity model [*Grand*, 2002]. While the MoMa array was not aligned exactly with the great circle path of these event-station pairs, it is close enough that the source-side *SPdKS* paths are only separated laterally by a ~3° (~180 km). The receiver-side *SPdKS* paths are more dispersed (~10° lateral spacing).

[51] Previous studies [*Thorne and Garnero*, 2004; *Rondenay and Fischer*, 2003; *Garnero et al.*, 1998] have consistently detected ULVZs in the Pacific region sampled by the source-side paths of these events; results for the CMB under the portion of North America sampled by these receiver-side paths are more ambiguous. Three-dimensional shear velocity models of the lower mantle from global travel time tomography [*Grand et al.*, 1997; *Masters et al.*, 2000; *Mégnin and Romanowicz*, 2000; *Gu et al.*, 2001; *Masters et al.*, 2000; *Ritsema and van Heijst*, 2000; *Grand*, 2002] show higher velocities in the region sampled by the receiver-side paths and low velocities in the region sampled by the source-side paths (Figure 15). These two lines of evidence hint that a one-sided ULVZ model might be appropriate for the data presented here.

[52] *Thorne and Garnero* [2004] individually compared each of the traces in Figure 14 to reflectivity synthetics [*Fuchs and Müller*, 1971; *Müller*, 1985] for a variety of CMB boundary layer models; the best fitting 1-D models for each of these traces are shown in Figure 14. Six of the 10 traces are fit best by PREM and PREM-like models (thin "ULVZs" with density perturbations but no velocity perturbations). Two are fit best by thin ($h ≤ 10$ km) ULVZs with 1:1 V_P:V_S perturbation ratios. And two are fit best by models incorporating fairly strong ULVZs, core-rigidity zones (CRZs), or core-mantle transition zones (CMTZs). This is a lot of variety for 10 paths that nearly overlap for much of their sampling of the CMB along the source-side P_{diff} path, suggesting rapidly varying structure in that region.
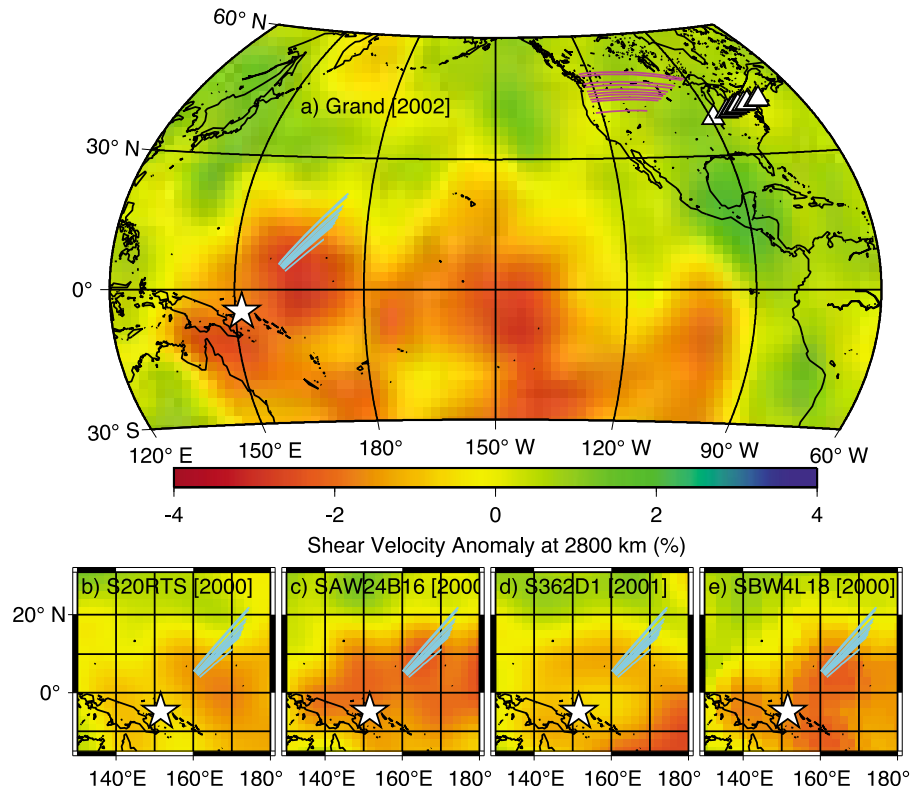
Figure 15. (a) Location of the source (white star) and receivers (white triangles) for the seismograms shown in Figure 14, as well as the expected *SPdKS* source-side (cyan lines) and receiver-side (magenta lines) sampling regions on the CMB, plotted on the 2800 km deep slice of the 3-D mantle shear wave anomaly model of *Grand* [2002]. The same source position and source-side P_{diff} paths are also plotted on the 2800 km deep slice of the 3-D mantle shear wave anomaly models of (b) *Mégnin and Romanowicz* [2000], (c) *Masters et al.* [2000], (d) *Ritsema and van Heijst* [2000], and (e) *Gu et al.* [2001], all compiled from the Reference Earth Model Web site (http://mahi.ucsd.edu/Gabi/rem.html).

[53] If we look at the 10 traces together (Figure 14) and compare them to the various 2-D modeling results presented in section 3, we notice that (1) there is only one *SKS* pulse and (2) the *SPdKS* arrival seems to comprise two pulses. The first *SPdKS* pulse is very close to that predicted for PREM, while the second is delayed by ~3.5 s relative to PREM *SPdKS*. This resembles the synthetic seismograms for models with P_{diff} inception in PREM followed by propagation into a proximal ULVZ (see section 3.4 and Figure 13). The *SPdKS* source-side paths on the CMB seem to begin within a region of large negative shear velocities and cross a strong shear velocity gradient in several 3-D *S* velocity models (Figure 15). The data in Figure 14 therefore suggest that a ULVZ is present within the region of the large lateral shear velocity gradient. This would be consistent with the proposal by *Williams et al.* [1998] that ULVZs are correlated with the hot spot source regions on the CMB and the observation of geographic correlation between hot spots and deep mantle lateral shear velocity gradients [*Thorne et al.*, 2004; *Garnero et al.*, 2007; *Garnero and McNamara*, 2008]. Our results are also consistent with the high lateral variability in CMB structure identified in this region by *Thorne and Garnero* [2004].

[54] If the *SPdKS* with PREM arrival time is due to receiver-side structure and the later *SPdKS* arrival is due to a P_{diff} inception within a source-side ULVZ, then using the 3.5 s relative delay of the second *SPdKS* with Figure 10 imposes some minimum constraints on the properties of the source-side ULVZ. It can have a minimum ULVZ strength (thickness multiplied by *P* velocity perturbation) of ~175 km % if the ULVZ is one-sided with full length. Based on *SPdKS* delay alone, it can also have greater ULVZ strength for laterally narrower ULVZ models, but it requires very strong ULVZs (greater than 400 km %) in order for ULVZs with lengths smaller than ~800 km to produce a large enough *SPdKS* travel time delay. Following *Stutzmann et al.* [2000], we note that if the P_{diff} inception point is within the ULVZ, the lack of a strong *SPKS* in Figure 14 indicates that the ULVZ is probably not as strong as 400 km % and therefore is probably longer than 800 km.

4.3. Comparison With Other 2-D Modeling of ULVZs

[55] *Helmberger et al.* [1996] used generalized ray synthetics to study the effect of one-sided ULVZ models on *SPdKS* while *Wen and Helmberger* [1998] used a hybrid method to model 2-D ULVZ structures. Between them, *Helmberger et al.* [1996] and *Wen and Helmberger* [1998] capture many of the same fundamental observations about the effect of 2-D ULVZ structures on *SKS*–*SPdKS* waveforms that we find in this work. We therefore provide inde-

pendent support to these previous results since the generalized ray, hybrid, and pseudospectral methods used by these three studies were all very different. Our results are distinguished by three unique findings. First, the observations of dual *SPdKS* for the finite length ULVZ models that begin just beyond the P_{diff} inception point offer a glimpse at more complex aspects of the 2-D behavior of *SPdKS*. Second, the production of Figure 10 offers a useful tool for examining the trade-offs between different aspects of the ULVZ parameterization in a quantitative way. Third, our approach provides a new, independent, and robust estimate of the spatial sensitivity of *SPdKS* at the CMB, something that cannot be found in the literature to date.

4.4. Implications for ULVZ Hypotheses

[56] In section 1, several hypotheses for the origin of ULVZs on the CMB were mentioned: partial melt, chemical heterogeneity (due to subducted slabs or iron enrichment from the core), phase transitions between perovskite and postperovskite, and outer core "sediments" collecting on the CMB. Here we consider whether the results from this study help to discriminate between these hypotheses.

[57] The use of *SPdKS* alone can provide two constraints that may be useful in distinguishing the possible causes of ULVZs. First, 2-D modeling provides limits on the horizontal spatial scale over which the ULVZ originating process must be occurring. All processes that create velocity anomalies detectable by *SPdKS* must occur on a lateral scale greater than 100 km. This may be a constraint useful in distinguishing between geodynamic models of ULVZ formation [see, e.g., *Garnero and McNamara*, 2008]. Second, we may be able to provide constraints on *P* velocities at the base of the mantle using the inception point for *SPdKS* events in a data section. For 2-D structures, the difference between the inception epicentral distances for two *SPdKS* events may help pin down the range of *P* velocities to which the *SPdKS* wave is exposed. This may be useful in distinguishing between different models of composition (iron or calcium or aluminum content in the magnesium silicate) and phase (perovskite versus postperovskite versus partial melt) at the base of the mantle.

[58] Using *SPdKS* alone, we can provide direct constraints only on combinations of ULVZ material properties (seismic velocities and density) and dimensions (thickness and lateral dimensions). It may be possible, however, to constrain individual material and dimensional properties of ULVZs by incorporating more phases. For example, stacks of short-period *ScP*, *ScS*, and *PcP* precursors and postcursors can tease apart ULVZ thickness versus *P* velocity, *S* velocity, and density perturbations [*Rost and Revenaugh*, 2003; *Avants et al.*, 2006]. It would be an interesting challenge in experiment design to create arrays of seismic receivers that, given the Earth's natural distribution of earthquake sources, would allow the same patch of CMB to be sampled by multiple core-sensitive phases, for example, both *SPdKS* and *ScP*, especially given that in order to constrain 2-D and 3-D aspects of variation in the CMB region 2-D and 3-D data sets will be required.

[59] This leads to the question: what constraints on ULVZ origin would be offered by a perfectly seismically constrained ULVZ with well determined thickness, lateral dimension, shape, seismic velocities, attenuation, and densities? Can

partial melting be distinguished from iron-enriched postperovskite or other chemical heterogeneities with perfect seismic knowledge? A full investigation of this question is beyond the scope of this paper, but *Lay and Garnero* [2008] suggest that it is hard to seismically distinguish between iron-enriched postperovskite and partial melting as origins for ULVZs. For any given hypothesis, it seems likely that the uncertainties in chemical composition, equations of state, and thermal state of the CMB will combine to allow a range of viable ULVZ models that would satisfy the seismic parameters. It is still useful, however, to attempt to combine seismic constraints with those from mineral physics, geochemistry, and geodynamics modeling to narrow the range of possibilities.

5. Conclusions

[60] Seismic wave propagation through two-dimensional core-mantle boundary ultralow-velocity zones is modeled using a global pseudospectral algorithm. Seismograms are synthesized for several types of ULVZ models, focusing on *SKS* and the related *SPdKS*/*SKPdS* phase that results from the intersection of the *SKS* wave with the CMB at the P_{diff} inception slowness. One-dimensional models with sharp and gradational upper boundaries and one-sided two-dimensional models with different quasi-1-D CMB structures on the source and receiver sides of the CMB are run to provide a baseline for comparison with other 2-D models. *SPdKS* travel times are shown to be sensitive mainly to the integrated vertical velocity structure of the ULVZ and only marginally to vertical velocity gradients within that profile. For nongradational ULVZs, *P* to *S* conversions at the top of the ULVZ result in the appearance of a high-amplitude *SKS* precursor in the synthetic seismograms, although only if the ULVZ is strong enough to produce an observable time separation between the two phases. The absence of such *SKS* precursors in data indicates that ULVZs in the Earth are either weaker than 300 km %, where ULVZ strength is parameterized as the ULVZ thickness multiplied by the average *P* velocity perturbation, or that they exhibit gradational velocity perturbations. For strong ULVZs, different velocity structures on the source and receiver sides of the CMB result in two *SPdKS* arrivals on the synthetic seismograms.

[61] Finite length 2-D ULVZ models are used to test the sensitivity of the *SPdKS* travel time and waveform to different portions of the *P* diffracted wave path and to explore the minimum length necessary for a ULVZ to produce observable changes in *SPdKS*. The *SPdKS* traveltimes and waveforms are completely insensitive to ULVZ structures placed at the exit points of P_{diff} to the core for epicentral distances greater than 115°. The *SPdKS* traveltime and waveforms, however, are strongly affected by 6° long (~360 km long) ULVZs placed along the P_{diff} path but ~2° (120 km) beyond the P_{diff} inception point. Finally, sensitivity to a ULVZ centered on the P_{diff} inception point is strongly dependent on the length of the ULVZ. We find that measurable *SPdKS* travel time delays are caused by ULVZs that have a length of at least 100 km, and that these delays increase progressively with increasing ULVZ length to reach values corresponding to the full one-sided ULVZ. Therefore, ULVZ length is an important variable, in addition to ULVZ

thickness and velocity, that contributes to the nonuniqueness of *SPdKS* time delays.

[62] Our results give three tools useful for identifying and characterizing 2-D ULVZ structures, all most useful if array data in something resembling a 2-D geometry is available. First, dual *SPdKS* pulses on a seismogram indicate exposure to at least two different CMB velocity structures. If the two *SPdKS* pulses are similar in amplitude, they probably indicate different quasi-1-D velocity structures on the source and receiver-side CMB. If the first pulse is PREM-like and significantly smaller than the second ULVZ-like *SPdKS*, it may indicate P_{diff} inception outside of and propagation into a ULVZ. Second, a strong *SKS* precursor probably indicates a very strong ULVZ with a sharp upper boundary. If the precursor is similar in amplitude to the *SKS* pulse, it indicates similarly strong ULVZ structure on both source and receiver-side CMB regions, and if the precursor is smaller than the *SKS* pulse, it may indicate a ULVZ on only the source or receiver side of the CMB. We note, however, that density perturbations in the ULVZ can also affect (although to second order) the relative amplitude between *SKS* and its precursors, so one should be cautious when interpreting these observations. Third, we present a graph of mean *SPdKS* delays relative to PREM that provides constraints on minimum ULVZ strength and length combinations required to produce a given travel time delay, which is more restrictive the greater the delay. Combining the results presented here with those from other studies of CMB-sensitive phases may lead to an improved characterization of fine-scale CMB structure.

References

Avants, M., T. Lay, and E. J. Garnero (2006), A new probe of ULVZ *S*-wave velocity structure: Array stacking of *ScS* waveforms, *Geophys. Res. Lett.*, *33*, L07314, doi:10.1029/2005GL024989.

Bataille, K., R. S. Wu, and S. M. Flatte (1990), Inhomogeneities near the core-mantle boundary evidenced from scattered waves: A review, *Pure Appl. Geophys.*, *132*(1–2), 151–173, doi:10.1007/BF00874361.

Berryman, J. G. (2000), Seismic velocity decrement ratios for regions of partial melt in the lower mantle, *Geophys. Res. Lett.*, *27*(3), 421–424, doi:10.1029/1999GL008402.

Blanch, J. O., J. O. A. Robertsson, and W. W. Symes (1995), Modeling of a constant Q: Methodology and algorithm for an efficient and optimally inexpensive viscoelastic technique, *Geophysics*, *60*(1), 176–184, doi:10.1190/1.1443744.

Braña, L., and G. Helffrich (2004), A scattering region near the core-mantle boundary under the North Atlantic, *Geophys. J. Int.*, *158*(2), 625–636, doi:10.1111/j.1365-246X.2004.02306.x.

Buffett, B. A., E. J. Garnero, and R. Jeanloz (2000), Sediments at the top of Earth's core, *Science*, *290*(5495), 1338–1342, doi:10.1126/science.290.5495.1338.

Bukowinski, M. S. T., and S. Akber-Knutson (2005), The role of theoretical mineral physics in modeling the Earth's interior, in *Earth's Deep Mantle; Structure, Composition, and Evolution, Geophys. Monogr.*

Ser., vol. 160, edited by R. D. van der Hilst et al., pp. 137–163, AGU, Washington, D. C.

Choy, G. L. (1977), Theoretical seismograms of core phases calculated by frequency-dependent full wave theory, and their interpretation, *Geophys. J. R. Astron. Soc.*, *51*(2), 275–312.

Cormier, V. F. (2000), D″ as a transition in the heterogeneity spectrum of the lowermostmantle, *J. Geophys. Res.*, *105*, 16,193–16,205, doi:10.1029/2000JB900141.

Cormier, V. F., and P. G. Richards (1988), Spectral synthesis of body waves in Earth models specified by vertically varying layers, in *Seismological Algorithms; Computational Methods and Computer Programs*, edited by D. J. Doornbos, pp. 3–45, Academic, London.

Crotwell, H. P., T. J. Owens, and J. Ritsema (1999), The TauP Toolkit: Flexible seismic travel-time and ray-path utilities, *Seismol. Res. Lett.*, *70*(2), 154–160.

Dziewonski, A. M., and D. L. Anderson (1981), Preliminary reference Earth model, *Phys. Earth Planet. Inter.*, *25*(4), 297–356, doi:10.1016/0031-9201(81)90046-7.

Fornberg, B. (1988), The pseudospectral method: Accurate representation of interfaces in elastic wave calculations, *Geophysics*, *53*(5), 625–637, doi:10.1190/1.1442497.

Fornberg, B. (1996), *A Practical Guide to Pseudospectral Methods*, Cambridge Univ. Press, New York.

Fuchs, K., and G. Müller (1971), Computation of synthetic seismograms with the reflectivity method and comparison with observations, *Geophys. J. R. Astron. Soc.*, *23*(4), 417–433.

Furumura, T., B. L. N. Kennett, and M. Furumura (1998), Seismic wavefield calculation for laterally heterogeneous whole earth models using the pseudospectral method, *Geophys. J. Int.*, *135*(3), 845–860, doi:10.1046/j.1365-246X.1998.00682.x.

Garnero, E. J. (2004), A new paradigm for Earth's core-mantle boundary, *Science*, *304*(5672), 834–836, doi:10.1126/science.1097849.

Garnero, E. J., and D. V. Helmberger (1995), A very slow basal layer underlying large-scale low-velocity anomalies in the lower mantle beneath the pacific: evidence from core phases, *Phys. Earth Planet. Inter.*, *91*(1–3), 161–176, doi:10.1016/0031-9201(95)03039-Y.

Garnero, E. J., and D. V. Helmberger (1996), Seismic detection of a thin laterally varying boundary layer at the base of the mantle beneath the central-Pacific, *Geophys. Res. Lett.*, *23*(9), 977–980, doi:10.1029/95GL03603.

Garnero, E. J., and D. V. Helmberger (1998), Further structural constraints and uncertainties of a thin laterally varying ultralow-velocity layer at the base of the mantle, *J. Geophys. Res.*, *103*, 12,495–12,509, doi:10.1029/98JB00700.

Garnero, E. J., and R. Jeanloz (2000a), Fuzzy patches on the Earth's core-mantle boundary?, *Geophys. Res. Lett.*, *27*(17), 2777–2780, doi:10.1029/2000GL008498.

Garnero, E. J., and R. Jeanloz (2000b), Earth's enigmatic interface, *Science*, *289*(5476), 70–71, doi:10.1126/science.289.5476.70.

Garnero, E. J., and A. K. McNamara (2008), Structure and dynamics of Earth's lower mantle, *Science*, *320*, 626–628, doi:10.1126/science.1148028.

Garnero, E. J., S. P. Grand, and D. V. Helmberger (1993), Low P-wave velocity at the base of the mantle, *Geophys. Res. Lett.*, *20*(17), 1843–1846, doi:10.1029/93GL02009.

Garnero, E. J., J. Revenaugh, Q. Williams, T. Lay, and L. H. Kellogg (1998), Ultralow velocity zone at the core-mantle boundary, in *The Core-Mantle Boundary Region, Geodyn. Ser.*, vol. 28, edited by M. Gurnis, M. E. Wysession, E. Knittle, and B. A. Buffett, pp. 319–334, AGU, Washington, D. C.

Garnero, E. J., T. Lay, and A. K. McNamara (2007), Implications of lowermantle structural heterogeneity for existence and nature of whole-mantle plumes, in *Plates, Plumes, and Planetary Processes*, edited by G. R. Foulger and D. M. Jurdy, *Spec. Pap. Geol. Soc. Am.*, *430*, 79–191.

Grand, S. P. (2002), Mantle shear-wave tomography and the fate of subducted slabs, *Philos. Trans. R. Soc.*, *360*, 2475–2491, doi:10.1098/rsta.2002.1077.

Grand, S. P., R. D. van der Hilst, and S. Widiyantoro (1997), Global seismic tomography: A snapshot of convection in the Earth, *GSA Today*, *7*(4), 1–7.

Gu, Y. J., A. M. Dziewonski, W. Su, and G. Ekström (2001), Models of the mantle shear velocity and discontinuities in the pattern of lateral heterogeneities, *J. Geophys. Res.*, *106*(B6), 11,169–11,200, doi:10.1029/2001JB000340.

Helmberger, D., S. Ni, L. Wen, and J. Ritsema (2000), Seismic evidence for ultralow-velocity zones beneath Africa and eastern Atlantic, *J. Geophys. Res.*, *105*, 23,865–23,878, doi:10.1029/2000JB900143.

Helmberger, D. V., E. J. Garnero, and X. Ding (1996), Modeling two-dimensional structure at core-mantle boundary, *J. Geophys. Res.*, *101*, 13,963–13,972, doi:10.1029/96JB00534.

Helmberger, D. V., L. Wen, and X. Ding (1998), Seismic evidence that the source of the iceland hotspot lies at the core-mantle boundary, *Nature*, 396(6708), 251–255, doi:10.1038/24357.

Jeanloz, R., and Q. Williams (1998), The core-mantle boundary region, in *Ultrahigh-Pressure Mineralogy: Physics and Chemistry of the Earth's Deep Interior, Rev. Mineral.*, vol. 37, edited by R. J. Hemley, pp. 241–259, Mineral. Soc. of Am., Washington, D. C.

Knittle, E. (1998), The solid/liquid partitioning of major and radiogenic elements at lower mantle pressures: Implications for the core-mantle boundary region, in *The Core-Mantle Boundary Region, Geodyn. Ser.*, vol. 28, edited by M. Gurnis et al., pp. 119–130, AGU, Washington, D. C.

Kosloff, D., and D. Kessler (1990), Seismic numerical modeling, in *Tomographie Ocenographique et Geophysique*, edited by Y. Desaubies, A. Tarantola, and J. Zinn-Justin, pp. 249–312, Elsevier Sci., New York.

Lay, T., and E. J. Garnero (2008), Reconciling the post-perovskite phase with seismological observations of lowermost mantle structure, in *Post-perovskite, The Last Mantle Phase Transition*, edited by K. Hirose et al., pp. 129–154, AGU, Washington, D. C.

Manga, M., and R. Jeanloz (1996), Implications of a metal-bearing chemical boundary layer in D″ for mantle dynamics, *Geophys. Res. Lett.*, 23(22), 3091–3094, doi:10.1029/96GL03021.

Mao, W. L., H. K. Mao, W. Sturhahn, J. Zhao, V. B. Prakapenka, Y. Meng, J. Shu, Y. Fei, and R. J. Hemley (2006), Iron-rich post-perovskite and the origin of ultralow-velocity zones, *Science*, 312(5773), 564–565, doi:10.1126/science.1123442.

Masters, G., G. Laske, H. Bolton, and A. Dziewonski (2000), The relative behavior of shear velocity, bulk sound speed, and compressional velocity in the mantle; implications for chemical and thermal structure, in *Earth's Deep Interior: Mineral Physics and Tomography From the Atomic to the Global Scale, Geophys. Monogr. Ser.*, vol. 117, edited by S.-I. Karato et al., pp. 64–86, AGU, Washington, D. C.

Mégnin, C., and B. Romanowicz (2000), The threedimensional shear velocity structure of the mantle from the inversion of body, surface and highermode waveforms, *Geophys. J. Int.*, 143(3), 709–728, doi:10.1046/j.1365-246X.2000.00298.x.

Müller, G. (1985), The reflectivity method; A tutorial, *J. Geophys.*, 58(1–3), 153–174.

Murakami, M., K. Hirose, K. Kawamura, N. Sata, and Y. Ohishi (2004), Post-perovskite phase transition in $MgSiO_3$, *Science*, 304(5672), 855–858, doi:10.1126/science.1095932.

Ni, S., V. F. Cormier, and D. V. Helmberger (2003), A comparison of synthetic seismograms for 2D structures: Semianalytical versus numerical, *Bull. Seismol. Soc. Am.*, 93(6), 2752–2757, doi:10.1785/0120030011.

Nielsen, P., F. If, P. Berg, and O. Skovgaard (1994), Using the pseudospectral technique on curved grids for 2D acoustic forward modelling, *Geophys. Prospect.*, 42(4), 321–341, doi:10.1111/j.1365-2478.1994.tb00213.x.

Revenaugh, J., and R. Meyer (1997), Seismic evidence of partial melt within a possibly ubiquitous low-velocity layer at the base of the mantle, *Science*, 277(5326), 670–673, doi:10.1126/science.277.5326.670.

Ritsema, J., and H. J. van Heijst (2000), Seismic imaging of structural heterogeneity in Earth's mantle: Evidence for large-scale mantle flow, *Sci. Progress*, 83, 243–259.

Robertsson, J. O. A., J. O. Blanch, and W. W. Symes (1994), Viscoelastic finite-difference modeling, *Geophysics*, 59(9), 1444–1456, doi:10.1190/1.1443701.

Rondenay, S., and K. M. Fischer (2003), Constraints on localized core-mantle boundary structure from multichannel, broadband *SKS* coda analysis, *J. Geophys. Res.*, 108(B11), 2537, doi:10.1029/2003JB002518.

Ross, A. R., H. Thybo, and L. N. Solidilov (2004), Reflection seismic profiles of the core-mantle boundary, *J. Geophys. Res.*, 109, B08303, doi:10.1029/2003JB002515.

Rost, S., and J. Revenaugh (2001), Seismic detection of rigid zones at the top of the core, *Science*, 294(5548), 1911–1914, doi:10.1126/science.1065617.

Rost, S., and J. Revenaugh (2003), Small-scale ultralow-velocity zone structure imaged by *ScP*, *J. Geophys. Res.*, 108(B1), 2056, doi:10.1029/2001JB001627.

Shim, S.-H. (2005), Stability of $MgSiO_3$ perovskite in the lower mantle, in *Earth's Deep Mantle: Structure, Composition, and Evolution, Geophys. Monogr. Ser.*, vol. 160, edited by R. D. van der Hilst et al., pp. 261–282, AGU, Washington, D. C.

Stutzmann, E., L. Vinnik, A. Ferreira, and S. Singh (2000), Constraint on the S-wave velocity at the base of the mantle, *Geophys. Res. Lett.*, 27(11), 1571–1574, doi:10.1029/1999GL010984.

Tackley, P. J. (1998), Three-dimensional simulations of mantle convection with a thermo-chemical basal boundary layer; D″?, in *The Core-Mantle Boundary Region, Geodyn. Ser.*, vol. 28, edited by M. Gurnis et al., pp. 231–253, AGU, Washington, D. C.

Tackley, P. J., S. Xie, T. Nakagawa, and J. W. Hernlund (2005), Numerical and laboratory studies of mantle convection: Philosophy, accomplishments, and thermochemical structure and evolution, in *Earth's Deep Mantle: Structure, Composition, and Evolution, Geophys. Monogr. Ser.*, vol. 160, edited by R. D. van der Hilst et al., pp. 83–99, AGU, Washington, D. C.

Tessmer, E., D. Kosloff, and A. Behle (1992), Elastic wave propagation simulation in the presence of surface topography, *Geophys. J. Int.*, 108(2), 621–632, doi:10.1111/j.1365-246X.1992.tb04641.x.

Thomas, C., J.-M. Kendall, and J. Lowman (2004), Lower-mantle seismic discontinuities and the thermal morphology of subducted slabs, *Earth Planet. Sci. Lett.*, 225(1–2), 105–113, doi:10.1016/j.epsl.2004.05.038.

Thorne, M. S., and E. J. Garnero (2004), Inferences on ultralow-velocity zone structure from a global analysis of *SPdKS* waves, *J. Geophys. Res.*, 109, B08301, doi:10.1029/2004JB003010.

Thorne, M. S., E. J. Garnero, and S. P. Grand (2004), Geographic correlation between hot spots and deep mantle lateral shear-wave velocity gradients, *Phys. Earth Planet. Inter.*, 146(1–2), 47–63, doi:10.1016/j.pepi.2003.09.026.

Tkalcic, H., and B. Romanowicz (2002), Short scale heterogeneity in the lowermost mantle: insights from *PcP-P* and *ScS-S* data, *Earth Planet. Sci. Lett.*, 201(1), 57–68, doi:10.1016/S0012-821X(02)00657-X.

Trampert, J., and R. D. van der Hilst (2005), Towards a quantitative interpretation of global seismic tomography, in *Earth's Deep Mantle: Structure, Composition, and Evolution, Geophys. Monogr. Ser.*, vol. 160, edited by R. D. van der Hilst et al., pp. 47–62, AGU, Washington, D. C.

Van Ark, E. M. (2007), Seismic and gravitational studies of melting in the mantle's thermal boundary layers, Ph.D, MIT-WHOI Jt. Program, Cambridge, Mass.

van der Hilst, R. D., S. Widiyantoro, K. C. Creager, and T. J. McSweeney (1998), Deep subduction and aspherical variations in P-wavespeed at the base of Earth's mantle, in *The Core-Mantle Boundary Region, Geodyn. Ser.*, vol. 28, edited by M. Gurnis et al., pp. 5–20, AGU, Washington, D. C.

van Thienen, P., J. van Summeren, R. D. van der Hilst, A. P. van den Berg, and N. J. Vlaar (2005), Numerical study of the origin and stability of chemically distinct reservoirs deep in Earth's mantle, in *Earth's Deep Mantle: Structure, Composition, and Evolution, Geophys. Monogr. Ser.*, vol. 160, edited by R. D. van der Hilst et al., pp. 117–136, AGU, Washington, D. C.

Vidale, J. E., and M. A. H. Hedlin (1998), Evidence for partial melt at the core-mantle boundary north of Tonga from the strong scattering of seismic waves, *Nature*, 391(6668), 682–685, doi:10.1038/35601.

Vidale, J., D. V. Helmberger, and R. W. Clayton (1985), Finite-difference seismograms for SH, *Bull. Seismol. Soc. Am.*, 75(6), 1765–1782.

Wen, L. (2000), Intense seismic scattering near the Earth's core-mantle boundary beneath the Comoros hotspot, *Geophys. Res. Lett.*, 27(22), 3627–3630, doi:10.1029/2000GL011831.

Wen, L., and D. V. Helmberger (1998), A two-dimensional *P-SV* hybrid method and its application to modeling localized structures near the core-mantle boundary, *J. Geophys. Res.*, 103, 17,901–17,918, doi:10.1029/98JB01276.

Wentzcovitch, R. M., N. L. Ross, and G. D. Price (1995), Ab initio study of $MgSiO_3$ and $CaSiO_3$ perovskites at lower-mantle pressures, *Phys. Earth Planet. Inter.*, 90(1–2), 101–112, doi:10.1016/0031-9201(94)03001-Y.

Williams, Q., and E. J. Garnero (1996), Seismic evidence for partial melt at the base of Earth's mantle, *Science*, 273(5281), 1528–1530, doi:10.1126/science.273.5281.1528.

Williams, Q., J. Revenaugh, and E. Garnero (1998), A correlation between ultra-low basal velocities in the mantle and hot spots, *Science*, 281(5376), 546–549, doi:10.1126/science.281.5376.546.

Wysession, M. E., K. M. Fischer, T. J. Clarke, G. I. Al-Eqabi, M. J. Fouch, P. J. Shore, R. W. Valenzuela, A. Li, and J. M. Zaslow (1996), Slicing into the Earth, *Eos Trans. AGU*, 77(37), 477, 480–482, doi:10.1029/96EO00316.

Zerr, A., A. Diegeler, and R. Boehler (1998), Solidus of Earth's deep mantle, *Science*, 281(5374), 243–246, doi:10.1126/science.281.5374.243.

V. F. Cormier, Physics Department, University of Connecticut, 2152 Hillside Rd., Storrs, CT 06269-3046, USA. (vernon.cormier@uconn.edu)

S. Rondenay and E. M. Van Ark, Department of Earth, Atmospheric and Planetary Sciences, Massachusetts Institute of Technology, 77 Massachusetts Ave. 54-618, Cambridge, MA 02139, USA. (rondenay@mit.edu; emilyva@alum.mit.edu)